UNIVERSITÄT BONN
Physikalisches Institut

Top Quark Mass Measurement using Lepton Transverse Momenta at ATLAS

von
Jan André Stillings

The Large Hadron Collider will produce a large number of top-antitop quark pairs and therefore allow the measurement of the top quark properties with high precision. Methods which are largely independent of a good calibration of the jet energies are favoured for the early data-taking. The determination of the top quark mass using the lepton transverse momentum is one such method.
Three methods were studied to investigate their suitability for ATLAS: fits of the mean and median lepton transverse momenta as functions of the top quark mass and a parametrisation of the lepton transverse momentum spectrum's shape. The methods were applied to electrons and muons independently and investigated for both dileptonic and lepton+jets top quark decays. An estimation of the statistical uncertainty for the top quark mass determination with an initial dataset of 200 pb^{-1} has been made.

Post address:
Nussallee 12
53115 Bonn
Germany

BONN-IB-2009-06
Bonn University
July 2009

UNIVERSITÄT BONN
Physikalisches Institut

Top Quark Mass Measurement using Lepton Transverse Momenta at ATLAS

von
Jan André Stillings

Dieser Forschungsbericht wurde als Diplomarbeit von der Mathematisch - Naturwissenschaftlichen Fakultät der Universität Bonn angenommen.

Angenommen am:	09.04.2009
Referent:	Prof. Dr. Ian C. Brock
Korreferent:	Prof. Dr. Hartmut Schmieden

Contents

Chapter 1

Introduction

The Standard Model of particle physics describes three of the four fundamental interactions and the elementary particles from which all visible matter in the universe is built. High energy physics tries to verify, to complete and to extend this very successful theory using the newest available experimental data. Various extensions of the Standard Model were introduced since its postulation in the 1960s. The discovery of tau leptons and new quarks had to be included into the theory. Current work is done on implementing a consistent handling of neutrino masses within the Standard Model. The theory is not yet complete but has shown itself to be flexible enough to assimilate new findings and corrections. Also the Standard Model allowed predictions on particles not yet found. A current prominent example is the Higgs boson which is required by the theory to explain the masses of the particles, in particular the force carriers of the weak force: W and Z.

To probe the Standard Model to a new level of precision and to find the Higgs boson, the Large Hadron Collider (LHC) has been built. It will start operation in 2009 after a long journey of planning, development and construction. The LHC is planned to accelerate protons up to energies of 7 TeV and to collide them with $\sqrt{s} = 14\,\mathrm{TeV}$ centre of mass energy available to generate Standard Model reactions and physics beyond the successful theory.

The top quark is the heaviest particle in the Standard Model which is the main reason for its late discovery in 1995 at the Tevatron collider. The top quark was already postulated in 1977 together with the discovery of its partner, the bottom quark. Until the construction of the Tevatron, no experiment could generate high enough energy to generate the mass of the top quark. Now the collider is still the only place where top quarks can be observed. The current measured mass is

$$M_t = 173.1 \pm 0.6\,(\mathrm{stat.}) \pm 1.1\,(\mathrm{syst.})\,\mathrm{GeV/c^2}. \tag{1.1}$$

Due to its high mass the top quark plays a very important role in the Standard Model. First of all it is possible to constrain the Higgs mass with the precise knowledge of the top quark mass and the W boson mass. In Figure 1.1 the current

constraints are shown. These constraints from LEP and Tevatron experiments will

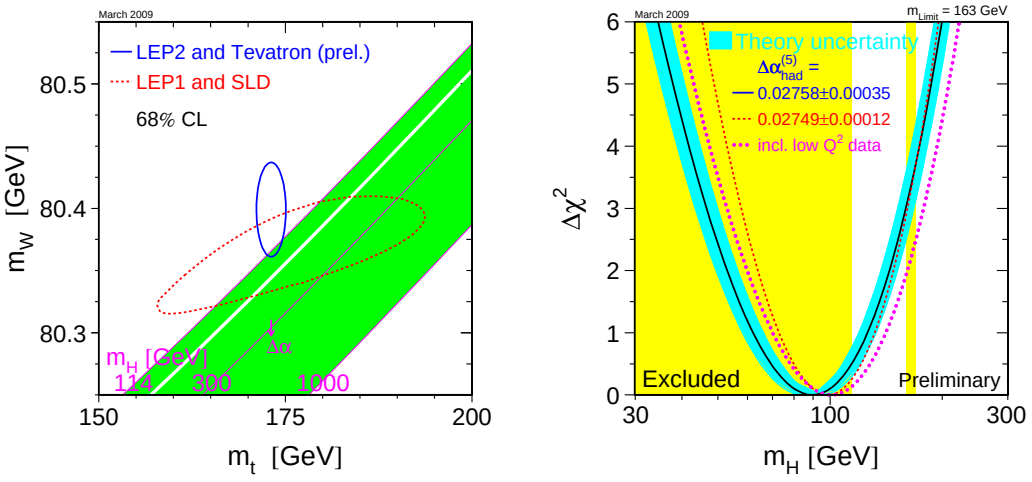

Figure 1.1: Combined constraints on the Higgs boson mass [1].

help the search for the Higgs boson at the LHC. Another important role of the top quark is the strong coupling to the Higgs boson. Due to this strong coupling, top quarks are present in many Higgs processes including possible discovery channels.

At the same time the top quark is a key background to processes for physics beyond the Standard Model. The precise knowledge of $t\bar{t}$ events and their production mechanism facilitates the work of extracting new physics like supersymmetry.

Due to its high collision energy the production cross section of $t\bar{t}$ pairs at the LHC will reach more than 850 pb at the target energy of 14 TeV. With the high number of collisions, more than eight million events are expected per year, making LHC a top quark factory. With the high statistics, the main experiments (ATLAS and CMS) aim to reduce the uncertainty on the top quark mass to less than $\pm 1\,\mathrm{GeV/c^2}$. The results from Tevatron have shown that the goal of high precision is best reached combining different methods of mass determination.

The main uncertainties of the top quark mass measurement at the beginning of the experiment originate from the calibration of the detector. The most prominent example is the jet energy scale (JES) which adds an uncertainty of $\pm\,0.73\,\mathrm{GeV/c^2}$ to the current Tevatron combined mass. The jet energy scale is used to relate the measured deposited energy from a jet in the calorimeter to the energy of the parton that produced the jet. It is important for most analyses. Due to the high amount of $t\bar{t}$ events at the LHC the systematic error will dominate most analysis results. Therefore it is useful to search for methods that do not rely heavily on these variables.

In this study the transverse momentum of leptonic top quark decay products is used

to measure the top quark mass. The top quark has a lifetime that is too short to allow hadronisation. This means that it decays directly before forming hadrons with other quarks. This is a unique feature of top quark decays and permits the mass of the top quark and the spin correlation of the $t\bar{t}$ pair to be infered from the properties of the decay products. Former studies have shown that the lepton transverse momentum is a good variable to measure the top quark mass. The aim of this study is to investigate the methods for this variable already used at Tevatron in the energy range of the LHC and the experimental environment of the ATLAS detector.

Three main methods are used in this thesis to infer a top quark mass dependence on the lepton transverse momentum: the transverse momentum spectra for different top quark masses were fitted directly and the mean as well as the median value of the lepton transverse momenta were studied. All of the three methods have the advantage of not depending on jet energy information. Jet energies are only used in the cut-based selection of $t\bar{t}$ events. Therefore the method is not so vulnerable to uncertainties on jet variables. This renders the applied methods less correlated to standard top quark mass measurements and can help to reduce the overall uncertainty. The mean value of the lepton transverse momentum has already been used at the CDF collaboration. The median is an alternative estimator for the top quark mass. The direct fit of lepton transverse momenta has also been studied at the CDF collaboration but results have not been published so far.

The variables used in the analysis are accessible in two different top quark decay channels: the dileptonic decays where both W bosons from the top quark decay leptonically and the lepton+jets decays where one W decays leptonically while the other decays hadronically and forms jets. The use of both channels has the advantage that one can perform cross-checks. The lepton+jets channel has a higher branching fraction and therefore includes higher statistics.

This thesis describes in a structured way the basics of the analysis, the applied methods and finally presents the results. In Chapter 2 a general introduction to the Standard Model including more detailed information about top quarks is given. Chapter 3 contains a description of the LHC and the ATLAS detector including the main detector components. In preparation for the application of the methods to official ATLAS Monte Carlo samples, a toolset has been built that can be used to perform distributed analyses on the LHC computing grid. An overview of the tool and the general analysis environment that has been used is given in Chapter 4. Chapter 5 deals with the Monte Carlo simulation explaining the used tools and listing the used samples. The selection of the two different studied $t\bar{t}$ decay channels is described in Chapter 6. It also shows cross-checks on the selected events and shortly describes possible sources of background. In Chapter 7 the different methods are explained and applied to the formerly selected events. The precision of the different methods is estimated and they are compared to each other. Chapter 8 finally summarises the studied methods and presents final conclusions.

Chapter 2

Theoretical Basics

In the field of high energy physics we try to understand the basic structure of matter. We search for both the elementary particles that our matter is built of and the interactions between them. So far the Standard Model is the accepted and, to a great extent, verified theory in the field and a basic introduction of it will be given in the following. With the Large Hadron Collider (LHC) we will not only probe this theory but also try to make it complete by discovering the Higgs boson as well as looking for evidence of physics beyond the Standard Model.

Hereafter the discovery of the top quark, its properties, its production at the LHC and also the types of its possible decays will be discussed in a bit more detail. The $t\bar{t}$ decay will be detailed in Chapter 6.

2.1 Standard Model

The Standard Model is a gauge theory describing the fundamental microscopic interactions between the elementary particles except for gravity. The underlying gauge symmetry has the form

$$\mathrm{SU}(3)_C \times \mathrm{SU}(2)_{I_W} \times \mathrm{U}(1)_Y . \tag{2.1}$$

This symmetry unifies two basic theories: the Glashow-Salam-Weinberg (GSW) theory for the weak and electromagnetic interactions and quantum chromodynamics (QCD) for strong interactions.

QCD is based on the $\mathrm{SU}(3)_C$ symmetry group. The corresponding conserved quantum number is called colour charge or just colour (C). It can have three different values called red, green and blue. The strong force is mediated by gauge bosons (spin 1), the gluons. Due to the non-abelian nature of $\mathrm{SU}(3)_C$, gluons interact with each other and hence carry colour[1]. Each gluon carries both colour and anti-colour

[1] Photons, the mediators of the electromagnetic force, don't carry electric charge.

resulting in eight different gluons. Additionally gluons are postulated to be massless and have no electric charge.

In the electroweak sector, the GSW theory uses the non-abelian $\mathrm{SU}(2)_{I_W} \times \mathrm{U}(1)_Y$ gauge group. Quantum numbers for this group are the weak isospin I_W and the hypercharge Y. In the electroweak case we have four gauge bosons mediating the forces, namely an uncharged photon, two charged W bosons and one uncharged Z boson. Unlike in QCD, $W^{\pm}$ and Z^0 bosons are found to have mass. To keep the theory gauge invariant the symmetry is spontaneously broken by introducing an additional scalar field, the Higgs field. This field is responsible for mass generation. After breaking the overall symmetry, the theory remains invariant under $\mathrm{U}(1)_{EM}$ transformations which describe the electromagnetic interactions. Therefore the photon is massless and the electromagnetic charge, Q, is the corresponding conserved quantum number.

Matter particles in the Standard Model are exclusively fermions (spin 1/2). They appear in both left-handed and right-handed states. Only neutrinos are supposed to be left-handed only in the Standard Model[2]. The left-handed fermions can be grouped into doublets according to their weak isospins:

$$\begin{pmatrix} \nu_e \\ e \end{pmatrix}_L \quad \begin{pmatrix} \nu_\mu \\ \mu \end{pmatrix}_L \quad \begin{pmatrix} \nu_\tau \\ \tau \end{pmatrix}_L$$
$$\begin{pmatrix} u \\ d \end{pmatrix}_L \quad \begin{pmatrix} c \\ s \end{pmatrix}_L \quad \begin{pmatrix} t \\ b \end{pmatrix}_L \tag{2.2}$$

These doublets are also called generations. Right-handed fermions only form isosinglets. Doublets in the upper row are leptons, in the lower row the quarks are organised. Each of the listed fermions also has an antiparticle with opposite charge and different hypercharge.

The electron (e) is the lightest charged lepton and was the first to be discovered by J.J. Thomson in 1897 [2]. Thomson concluded from experiments with cathode rays that they consist of single particles and already could determine the charge over mass ratio of the electrons. The electron has, like all charged leptons, an electric charge $Q = -1\mathrm{e}$ and a mass of 0.5 MeV. Its antiparticle is called positron.

Muons (μ) are rather exact copies of electrons despite their larger mass of 105.7 MeV. This mass difference was the basis for the discovery by Anderson and Neddermeyer in their extensive research of cosmic ray tracks [3]. Contrary to their lighter partners, muons are not stable and decay weakly into electrons and neutrinos with a lifetime of 2.2 µs.

[2] As experiments show small neutrino masses, the Standard Model has to be expanded. The current two models are to introduce Dirac neutrinos or a new type of particles called Majorana neutrinos.

The third and heaviest type of charged leptons are tau leptons (τ) or just taus. They were discovered by Martin Perl in 1974 with the Mark I detector at the SLAC e^+e^- collider [4, 5, 6]. Taus are the heaviest charged leptons with a mass of 1776.8 MeVand a lifetime of 290.6×10^{-15} s. Taus mostly decay to neutrinos, kaons, pions and other mesons but a fraction of about 35% also decays in 3-body decays to electrons or muons and neutrinos which were the discovery channels at Mark I.

All the previous mentioned charged leptons interact electromagnetically and weakly with other particles. They carry no colour charge and thus are not influenced by the strong force.

Mentioned briefly in the possible decay modes above is the second class of leptons called neutrinos. They occur in three different states named after their charged leptonic partners: electron neutrinos (ν_e), muon neutrinos (ν_μ) and tau neutrinos (ν_τ). Neutrinos carry neither electromagnetic charge nor colour and only interact weakly with other particles which makes their detection hard. The existence of neutrinos was first postulated by Wolfgang Pauli in 1930 to explain the non-discrete spectrum of beta decays. Experimentally the neutrino was only accessible after the development of nuclear reactors. Reines and Cowan finally found the electron neutrino in 1956[3] [9]. The Standard Model assumes all neutrinos to be massless which newer experiments contradict[4].

The second big group of massive particles are the quarks. Like neutrinos, their first appearance happened in theory. M. Gell-Mann and G. Zweig independently postulated the first quark model in 1964 [11, 12, 13] to explain the large and growing number of found hadrons. The experimental discovery of quarks started with the observation of the proton substructure in deep inelastic scattering experiments and was only final with the discovery of the top quark in 1995 [14, 15]. Quarks are the only particles that couple to all three interactions as they carry charge, colour and weak hypercharge. The properties of the quarks are given in Table 2.1.

A special conserved quantum number of quarks given in the table: the flavour. Up and down quarks are characterised by the third component of the isospin (I_z) while the other quark types have none ($I_z = 0$) and therefore their quark flavour is given. Similar quantum numbers also exist for leptons: the leptonic family number and the lepton number. The lepton number counts the leptons coming from an interaction vertex positively while antileptons are counted negatively. The leptonic family number is counted in the same way but only considering leptons of the same family. Leptonic family numbers and lepton numbers are also conserved in the Standard Model if we consider zero neutrino masses. Leptons in one family thus can not be directly changed into a lepton of a different family. This is only possible through an

[3] The muon neutrino was found by L.M. Lederman, J. Steinberger and M. Schwartz at the AGS experiment in Brookhaven [7]. The tau neutrino has only been detected in 2000 with the DONUT detector at Fermilab [8].

[4] Neutrino experiments have shown neutrino oscillations which imply a small mass on the neutrinos [10].

Quark	Charge	Mass	Flavour
Up	$+\frac{2}{3}$	1.5 to 3.3 MeV/c^2	$I_z = +\frac{1}{2}$
Down	$-\frac{1}{3}$	3.5 to 6.0 MeV/c^2	$I_z = -\frac{1}{2}$
Charm	$+\frac{2}{3}$	$1.27^{+0.07}_{-0.11}$ GeV/c^2	Charm = +1
Strange	$-\frac{1}{3}$	104^{+26}_{-34} MeV/c^2	Strangeness = -1
Top	$+\frac{2}{3}$	171.2 ± 2.1 GeV/c^2	Top = +1
Bottom	$-\frac{1}{3}$	$4.20^{+0.17}_{-0.07}$ GeV/c^2	Bottom = -1

Table 2.1: Quark Properties from [16].

intermediate particle like a $W^{\pm}$ boson. In case of neutrino oscillations this principle is violated. For the quarks the situation is different. In QCD the flavour is conserved like in the leptonic case though for the electroweak theory we have a breaking of this symmetry. In the theory the transition probability between quark types is given by the Cabibbo-Kobayashi-Maskawa (CKM) quark mixing matrix:

$$\begin{pmatrix} d' \\ s' \\ b' \end{pmatrix} \begin{pmatrix} V_{ud} & V_{us} & V_{ub} \\ V_{cd} & V_{cs} & V_{cb} \\ V_{td} & V_{ts} & V_{tb} \end{pmatrix} = \begin{pmatrix} d \\ s \\ b \end{pmatrix} \tag{2.3}$$

The CKM matrix connects the mass eigenstates of the quarks (d, s, b) to the corresponding weak eigenstates (d', s', b'), which are different in GSW. With the current best fit values one can see that transitions between the generations are suppressed while transitions between quarks inside a family are favoured:

$$\begin{pmatrix} 0.97419 \pm 0.00022 & 0.2257 \pm 0.0010 & 0.00359 \pm 0.00016 \\ 0.2256 \pm 0.0010 & 0.97334 \pm 0.00023 & 0.0415^{+0.0010}_{-0.0011} \\ 0.00874^{+0.00026}_{-0.00037} & 0.0407 \pm 0.0010 & 0.999133^{+0.000044}_{-0.000043} \end{pmatrix} \tag{2.4}$$

Details about the CKM matrix elements can be found in [16] and [17].

2.2 The Top Quark

2.2.1 Discovery of the Top Quark

In 1973 M. Kobayashi and T. Maskawa presented an extension to the electroweak theory that included a third generation of quarks[5] [18]. The first step to verify this theory was taken with the discovery of the bottom quark in 1977 at Fermilab [19]. Over the following years more and more physicists were convinced that a sixth quark was missing in the model and many experiments narrowed the constraints on the particle's mass. A first direct measurement was finally accomplished by the CDF and DØ collaborations at Fermilab in 1995 [14, 15].

[5]This extension made it possible to explain the CP symmetry violation in kaon decays which would not occur in the GSW model for four quarks.

2.2.2 Top Quark Properties

Due to the late discovery of the top quark and the low statistics compared to other quarks, some of its properties are not yet determined to high precision. Since the first candidate, the CDF and DØ collaborations have made big efforts to improve the knowledge about the top quark's main characteristics. The Tevatron accelerator remains at the present time the only facility capable of producing top quarks. The current status of the measurements as of the latest CDF and DØ publications [20, 21] will be summarised briefly.

Mass The top quark is the heaviest known elementary particle. Latest measurements of its mass from Tevatron give an average of

$$M_t = 173.1 \pm 1.3\,\mathrm{GeV/c^2}. \tag{2.5}$$

The given error splits up into various sources which can be summarised to systematics (± 1.1 GeV/c^2) and statistics (± 0.6 GeV/c^2). The used data is from two different Tevatron data taking periods, Run I and Run II, where Run II included a higher centre-of-mass energy and higher luminosity as well as detector upgrades. Run I data suffered from a large statistical error while the biggest contribution to the total error came from the uncertainty on the jet energy scale (JES). Both uncertainties were successfully reduced in the Run II analyses. Also in Run II a new analysis technique was applied in the CDF collaboration which uses the mean decay-length of B-tagged jets and the mean lepton transverse momentum which this study relies on. The impact of different analyses on the combined result is shown in Figure 2.1.

Lifetime In the Standard Model the lifetime of the top quark is predicted to be around $\tau \sim 4 \times 10^{-25}$ s, a very small value compared to other particles. This corresponds to a width of 1.5 GeV and a travelled distance of $c\tau \sim 1.5 \times 10^{-16}$ m. This distance cannot be directly measured but a first attempt to give a direct limit has been made from the CDF collaboration [22] using data of 318 pb^{-1}integrated luminosity. The applied method uses $t\bar{t}$ pairs decaying into leptons and jets to separate the $p\bar{p}$ collision point and the leptonic track. This delivers an upper limit on the travelled distance of the leptonically decaying top quark of $c\tau < 52.5$ µm with a confidence level of 95% which is consistent with a zero lifetime. Further studies on larger data samples were not presented so far.

Electric Charge Like all other up-type quarks in the Standard Model, the top quark is predicted to have a charge of $Q = +2/3$ e. The electric charges of the other quarks have been successfully determined at e^+e^- colliders. Since the so far built e^+e^- machines operated below the production threshold of $t\bar{t}$ pairs the charge has yet to be measured. The experiments at the Tevatron collider do not assign distinct b, $\bar{b}$ and $W^\pm$ to their corresponding mother products thus also allowing exotic decays

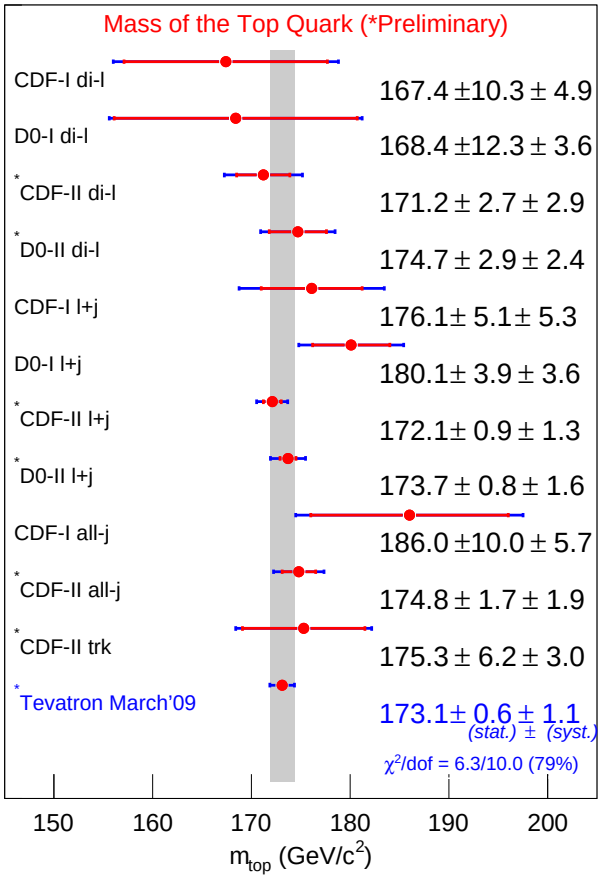

Figure 2.1: A Summary of the input measurements and resulting world average mass of the top quark. Different $t\bar{t}$ decay channels: di-l: dileptonic decay, l+j: decay into lepton and jets, all-j: full-hadronic decay. trk: Track based analysis [20].

such as $t \to W^+\bar{b}$. Such decays could be satisfied by models that suppose an exotic doublet of charge -1/3 e and -4/3 e quarks (Q_1, Q_4) [23]. Both the DØ and CDF collaborations worked on probing this model. DØ could exclude at 92% confidence level that the data sample is solely composed of Q_4 particles and determined an upper limit of $\rho < 0.80$ at 90% C.L. for the fraction of Q_4 quarks pairs in the data. With a different method CDF excluded a top quark charge of $Q = -4/3$ with 87% confidence level. Both measurements indicate agreement with the Standard Model predictions.

2.2.3 Top Quark Production at the Large Hadron Collider

The Large Hadron Collider (LHC) is planned to collide protons with a centre-of-mass energy of up to $\sqrt{s} = 14$ TeV. Due to the problems with the start-up in 2008,

the first longer data-taking period will limit the collision energy to $\sqrt{s} = 10$ TeV. At such energies it is not the protons that interact with each other but their subcomponents (partons), namely valence quarks (up and down), sea quarks and gluons. One can interpret the incoming protons as beams of quarks and gluons that collide. The partons carry a fraction, x, of the total momentum of the mother proton. The

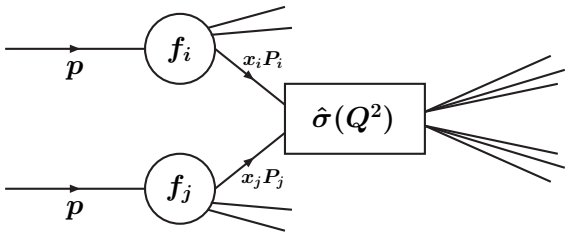

Figure 2.2: PDFs f_i, f_j in proton-proton collisions.

distribution of the longitudinal parton momenta, x_i, inside the proton is given by the parton distribution functions (PDF), $f_i(x_i, Q^2)$. They show a dependence on the momentum fraction, x_i and the square of the transferred transverse momentum, Q^2, which is the energy scale for an event. Together with the cross section of the hard scattering process the PDF determines the full cross section of the interaction. One big problem is that PDFs cannot be calculated analytically with pertubative QCD and thus have to be determined from experiments like deep-inelastic scattering. The PDFs used at LHC were measured in fixed target experiments and especially at the Tevatron and HERA colliders. By using the DGLAP equations[6] [24] it is possible to scale the PDFs to a higher energy scale, Q^2. Collaborations like CTEQ offer sets of PDF parametrisations for applications like the ATLAS event generation [25]. In Figure 2.3, two parametrisations are shown for different scales of Q^2. For $t\bar{t}$ production the events possess higher Q^2, like in the right figure. To produce a $t\bar{t}$ pair at rest, at least twice the top quark mass is needed as effective centre-of-mass energy in the partonic process:

$$\sqrt{\hat{s}} = \sqrt{(x_i P_i + x_j P_j)^2} \geq 2m_t \tag{2.6}$$

Setting $x_i \approx x_j \equiv x$ and assuming a top quark mass of 175 GeV/c^2 we can calculate typical momentum fractions for $p\bar{p}$ and pp colliders:

$$\begin{aligned} x &\approx \tfrac{2m_t}{\sqrt{2}} \\ &= 0.025 \qquad \text{LHC @ 14 TeV} \\ &= 0.18 \qquad \text{Tevatron Run II} \end{aligned} \tag{2.7}$$

With the value of the momentum fraction it is possible to estimate the dominating process in the creation of $t\bar{t}$ with the shown CTEQ graphs from Figure 2.3. For the higher momentum fraction x at Tevatron the valence quark PDFs are in the same

[6] Short for Dokshitzer-Gribov-Lipatov-Altarelli-Parisi QCD evolution equations

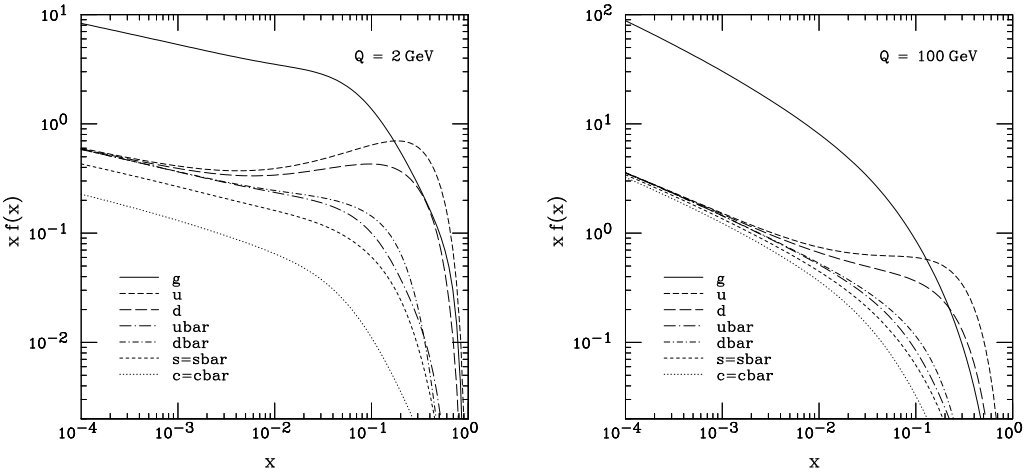

Figure 2.3: Two PDF parametrisations from CTEQ collaboration [25].

order and a bit higher than the gluon PDF. Thus the production at Tevatron is dominated by quark-antiquark annihilation. The process' Feynman graph is shown in Figure 2.4. Only about 15% of the $t\bar{t}$ pairs are created by gluon fusion processes

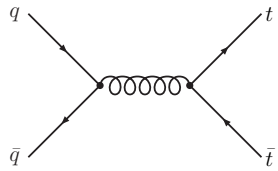

Figure 2.4: Feynman graphs for $t\bar{t}$ production from $q\bar{q}$ annihilation.

shown in Figure 2.5. Opposite to Tevatron the low momentum fraction necessary at the LHC create a dominating role of 90% of gluon-gluon fusion processes compared to quark-antiquark annihilation. The cases were x_i and x_j are asymmetric also contribute to the superior process as they provide incoming low-x gluons. All the above processes are mediated by the strong force.

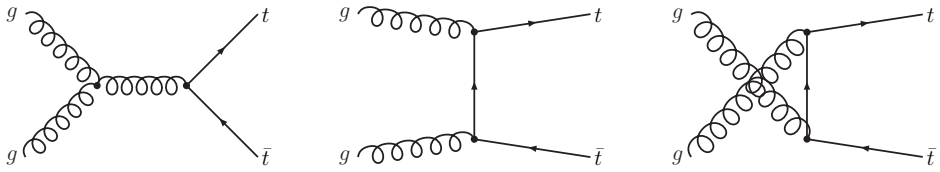

Figure 2.5: Feynman graphs for $t\bar{t}$ production with gg fusion.

To calculate the cross-sections the $t\bar{t}$ creation process is computed using the factorisation theorem to combine the described PDFs with the cross-sections for the hard processes between the partons. These hard processes are calculated with a

pertubative expansion in orders of the strong coupling constant, α_S. The Feynman diagrams above show the leading order (LO) of this expansion. Graphs in higher order contain radiative corrections, loops, etc. The cross section for $t\bar{t}$ production at the LHC for 14 TeV has been calculated with next-to-leading order (NLO) precision including next-to-leading logarithmic (NLL) soft-gluon resummation. A cross section of 883.90 ± 53 pb has been predicted [26]. For 10 TeV center-of-mass energy a lower cross-section of about 401 ± 24 pb has been computed. For the first year of running with its expected integrated luminosity of $200\,\mathrm{pb}^{-1}$ this leads to around 80 000 $t\bar{t}$ events. In the later running periods with 14 TeV at a luminosity of $10^{33}\,\mathrm{cm}^{-2}\,\mathrm{s}^{-1}$ about eight million $t\bar{t}$ events will be produced per year. Thus LHC will be a top quark factory assuring high statistics for data analysis.

It is also possible to create top quarks in weak interactions resulting in only single top quarks. The main production channels here are W gluon fusion (t-channel), associated production of a top quark and W boson (Wt) and s-channel production. The Feynman graphs for these channels are shown in Figure 2.6. The summed cross section for these events is estimated with 323 pb at 14 TeV centre-of-mass energy and 164 pb at 10 TeV[27, 28, 29, 30]. The discovery of this production channel has been reported by CDF and DØ very recently [31, 32].

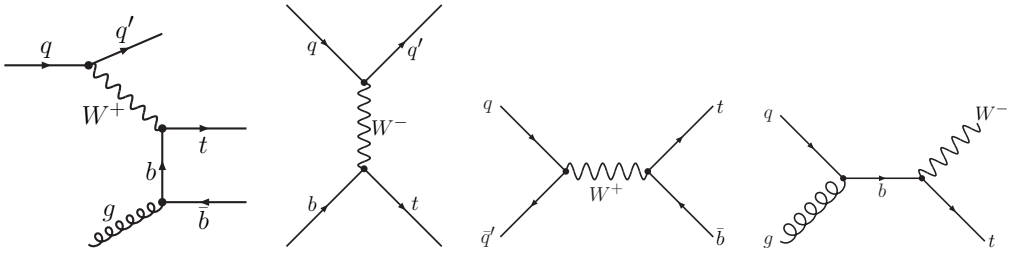

Figure 2.6: Feynman graphs for single top quark production. From left to right: two t-channel graphs, s-channel, Wt-channel.

2.2.4 Top Quark Decay

As described in Section 2.2.2 the top quarks have an average lifetime of

$$\tau \sim 4 \times 10^{-25}\mathrm{s} \tag{2.8}$$

and thus do not travel far enough to get detected by current detectors. To derive its properties anyhow it is therefore needed to measure the decay products that can give further information about their parent particles. Precise information about the decay of the top quark is thus needed.

Unlike other quarks, the top quark does not persist long enough to form a bound state and decays directly[7]. It decays nearly exclusively to a W boson and a b quark

[7]The b quark for example forms bound states with lower mass quarks to form a B hadron before decaying.

Figure 2.7: Feynman graphs for leptonic (left) and hadronic (right) top quark decays.

in a weak decay. This decay is called Cabibbo-favoured as the corresponding CKM matrix element is large compared to the ones of the other possible decays.

$$R = \frac{B(t \to Wb)}{B(t \to Wq)} = \frac{|V_{tb}|^2}{|V_{td}|^2 + |V_{ts}|^2 + |V_{tb}|^2} \approx 1 \tag{2.9}$$

A decay into a lepton is not possible due to the absent hadronisation and the charge conservation. The resulting W boson and b quark aren't stable particles either. The b quark hadronises into a B meson which then decays weakly into a D meson and finally into stable particles with a jet signature. The decay into a D meson is again Cabbibo-favoured as the CKM matrix element V_{ub} nearly vanishes. The W boson on the other hand decays in different channels into stable and unstable particles. It can either decay leptonically into a lepton (e, μ or τ) and its corresponding neutrino or hadronically into a quark and an antiquark. The corresponding Feynman diagrams are shown in Figure 2.7. Due to kinematical reasons, the quark-antiquark combinations in the hadronic decay are only composed of light quarks ($u\bar{d}$ and $c\bar{s}$).

Chapter 3

The ATLAS Experiment

This study has been performed within the framework of the ATLAS collaboration. ATLAS is one of the four detector experiments at the Large Hadron Collider that is currently being put into operation at CERN[1] in Geneva. In this chapter a brief description of the experiment will be given to illustrate the quantities used in the later analysis.

3.1 The Large Hadron Collider

The Large Hadron Collider (LHC) is a circular superconducting accelerator and collider built in the former LEP[2] tunnel [33, 34]. The accelerator has a circumference of about 27 km and is located about 100 m below the ground. The accelerator has eight arcs and straight sections of 528 m each, which are possible areas for experiments or utilities. Two interaction sections host the high luminosity multi-purpose detectors ATLAS and CMS. They aim at a peak luminosity of $10^{34}\,\mathrm{cm}^{-2}\,\mathrm{s}^{-1}$ in proton-proton collisions. Two other proton collision experiments aim at lower luminosities: LHCb will concentrate on bottom quark physics at $10^{32}\ \mathrm{cm}^{-2}\,\mathrm{s}^{-1}$ peak luminosity and TOTEM will measure the total cross section, elastic proton scattering and diffractive processes near the CMS experiment. In addition to protons, the LHC will also be able to collide heavy ions. A dedicated experiment called ALICE will operate at a peak luminosity of $10^{27}\ \mathrm{cm}^{-2}\,\mathrm{s}^{-1}$ in Pb-Pb operation and study these collisions.

To achieve the high intensities needed, the LHC will accelerate equally charged particles in two independent beam-pipes with opposite magnet dipole fields. To capture the beam from the pre-accelerator chain, accelerate it and store it at the projected peak energy of 7 TeV per proton, an RF system in the LHC of frequency 400.8 MHz is installed. The accelerator will store 2 808 bunches for each proton beam

[1] European Organisation for Nuclear Research; name derived from Conseil Européen pour la Recherche Nucléaire

[2] Large Electron Positron Collider (operation: 1989 to 2000)

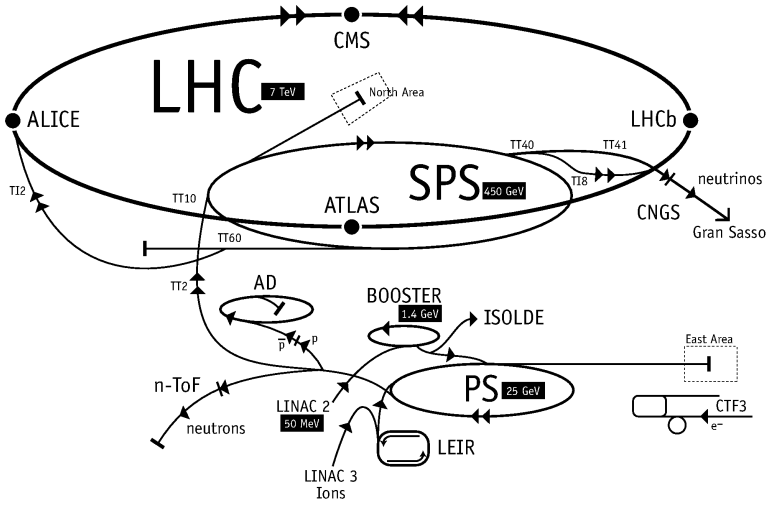

Figure 3.1: Accelerator chain of the Large Hadron Collider.

with a bunch length of 1.06 ns and a bunch spacing of 25 ns at maximum energy. Both the acceleration cavities and the guidance magnets of LHC use superconducting technologies. The dipoles are cooled down to temperatures of 1.9 K using superfluid helium to achieve a maximum central field strength of 8-8.5 T which is needed to bend the beams.

The proton beams are pre-accelerated by a chain of reused accelerators that were upgraded to meet the requirements of the LHC. The protons are produced in a duoplasmatron from hydrogen gas and injected into the Linac2 which accelerates the protons up to 50 MeV. In the following chain they are accelerated by the Proton Synchrotron Booster (PSB) to 1.5 GeV, by the Proton Synchrotron (PS) up to 25 GeV and finally by the Super Proton Synchrotron (SPS) to 450 GeV which is the injection energy for LHC.

A detailed description of the LHC can be found in the LHC design report [35, 36, 37].

3.2 Physical Observables

To describe, measure and calculate particle attributes in hadron collisions it is important to consider specific features of these events as explained in Section 2.2.3. As the colliding quarks and gluons carry a momentum fraction, x_i, of the proton, their initial momentum is not known[3] thus applying a Lorentz boost of unknown size to the event parallel to the beam axis. This affects all outgoing momenta $\vec{p}$. To acquire a variable independent from this boost in the z-direction hadron collider

[3] In e^+e^- collisions, the initial momentum is a known variable and useful for further calculations.

experiments usually refer to the transverse momentum

$$p_T = \sqrt{p_x^2 + p_y^2}. \tag{3.1}$$

The same constraint is valid for the missing energy of an event. As the incoming partons are expected to have approximately no transverse momentum, the corresponding sum of all outgoing particles has to vanish as well due to momentum conservation. As the detector is not able to trace some particles[4] it is possible to calculate this missing transverse momentum E_T^{miss} and to use it for event selection.

Positions inside the detector are usually given in cylindrical coordinates (r, θ, ϕ) with r as the radial distance from the beam axis and ϕ as the azimuthal angle which describes the direction perpendicular to the beam axis. Instead of the polar angle θ between the flight direction of the particle and the beam axis, the third coordinate is given in terms of the pseudorapidity

$$\eta = -\ln \tan \frac{\theta}{2}. \tag{3.2}$$

This variable has the advantage that differences in η are invariant under Lorentz boosts that especially occur in hadron collider events. A positive side effect of this representation is the steep rise of η in the area close to the beam axis. This area often contains a much higher particle density which makes a separation easier and leads to flatter distributions.

After defining η it is convenient to give distances in the η-ϕ plane. The distances are then defined as

$$\Delta R = \sqrt{\Delta\eta^2 + \Delta\phi^2}. \tag{3.3}$$

3.3 The ATLAS Detector

"A Toroidal LHC ApparatuS" (ATLAS) is one of the multipurpose detectors at the LHC. Figure 3.2 shows a generated overview of the detector and its main components. The dimensions are about 44 m in length and 25 m in height with a total weight of approximately 7 000 tons. The main systems of the detector are the inner detector, the calorimeters, the muon and the magnet system. The following short summary is a brief overview of the named systems which are described in detail in the ATLAS technical report [39].

3.3.1 Inner Detector

Surrounding the interaction point of ATLAS the Inner Detector (ID) is responsible for track reconstruction, momentum measurement, charge determination and

[4] Neutrinos pass the detector mostly without interaction.

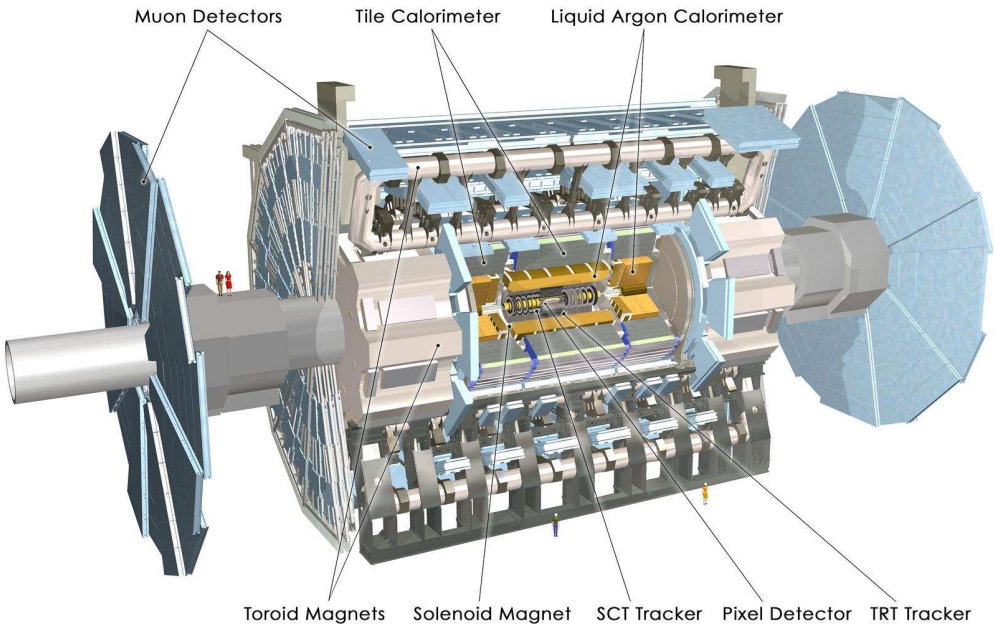

Figure 3.2: Computer-generated image of the ATLAS detector and its subsystems. [38]

primary as well as secondary vertex finding. The ID consists of three main components: the Pixel Detector, the Semiconductor Tracker (SCT) and the Transition Radiation Tracker (TRT). The whole ID is surrounded by a solenoid magnet which generates a field of about 2 T to ensure sufficient bending of particle tracks even at high momenta. The total length of the ID is 7 m with a diameter of 1.5 m. It covers a pseudorapidity range of $|\eta| < 2.5$.

The Pixel Detector is the component closest to the interaction point and consists of 1 744 pixel sensor modules with 47 232 pixels each. Due to overlaps 46 080 readout channels are available per module resulting in a total of 67 million pixels in the barrel and 13 million pixels in the endcap region. The modules are placed in three layers around the interaction point in the central region and on three disks in each of the forward regions. Together the layers detect at least three points per track with very high accuracy due to their small pixel size[5].

The SCT consists of four layers mounted in the barrel region and nine disks on each side in the forward regions. On the disks there are modules mounted radially on both sides which are rotated with respect to each other to permit precise determination of a z coordinate. Installed in the SCT are 8 448 modules in the barrel and 6 944 modules in the forward regions. Each module contains 768 readout strips with a constant 80 µm pitch. Together with the Pixel Detector the SCT provides an average of seven hits for a track offering high spatial resolution.

[5]The pixel size is 50 µm in the ϕ and 400/600 µm in the z direction.

To increase the number of measured track positions, without the downside of adding more dead material, the silicon detectors are enclosed by the TRT made from straw tubes. These tubes have a diameter of 4 mm and are enclosed by 35 µm thick multi-layer films which act as cathodes supplied with high voltage. They are filled with a gas mixture of 70% Xe, 27% CO_2 and 3% O_2. The signal is captured by a grounded anode wire in the middle and read out at the end[6]. In the barrel region the straws are mounted parallel to the beam pipe and have a length of 144 cm with a total of 73 straw planes. In the endcap regions the straw tubes are arranged radially in wheels with a length of 37 cm building up 160 straw planes. The TRT contains a total number of about 351 000 readout channels. It adds an average of 36 additional points to a track and improves the identification of electrons which create transition radiation in the foils between the planes.

3.3.2 Calorimeter

The calorimeter is the part of the detector responsible for energy measurement and particle identification. Additionally it is used to complete the tracking of particles and to determine the missing energy of an event. The calorimeter is divided in two major parts: the electromagnetic calorimeter (EM) that registers electromagnetic showers from electrons, positrons and photons and the hadronic calorimeter that registers hadronic showers resulting from jets. Each of the parts is again built out of subcomponents adjusted to the different pseudorapidity ranges they cover.

The EM calorimeter is divided into a barrel part and two wheel sections in the forward directions. Those components which cover the region of precision measurements ($|\eta| < 2.5$) have three layers and a higher granularity in contrast to the two layers in the forward regions. All the parts use liquid argon (LAr) as active detector material. Accordion shaped lead plates are used as absorber media and the readout is implemented with three copper layers of which the outer ones are set to high voltage while the inner layer allows a capacitive readout. Photons and electrons/positrons create electromagnetic showers in this part. The EM calorimeter in total is 22 to 24 radiation lengths thick to ensure small leakage into the hadronic calorimeter. Its energy resolution is dependent on the $|\eta|$ position and on the particle type. For electrons it is expected to reach [40]

$$\frac{\sigma(E)}{E} = \frac{9.3\%}{\sqrt{E}} \oplus 0.56\,\%\,[\mathrm{GeV}] \qquad \text{for } |\eta| = 0.3 \tag{3.4}$$

$$\frac{\sigma(E)}{E} = \frac{19.4\%}{\sqrt{E}} \oplus 0.43\,\%\,[\mathrm{GeV}] \qquad \text{for } |\eta| = 1.65. \tag{3.5}$$

The hadronic calorimeter is composed of three parts: the tile calorimeter directly outside the EM calorimeter envelope, the LAr hadronic end-cap calorimeter and the Forward Calorimeter. The tile calorimeter has a main part and two extensions which

[6] Anode readouts are located at both ends for the longer modules in the central region.

together cover the range of $0 < |\eta| < 1.7$. Steel is used as absorber and scintillating tiles as active material. The thickness is about two meters which corresponds to 9.1 interaction lengths. The LAr calorimeters in the end-cap region are wheel-shaped and divided by copper plates while LAr again is the active material. They share the LAr cryostats with the EM calorimeter wheels. The forward calorimeter has a compound design made of one copper plate for electromagnetic measurements and two modules made of tungsten. LAr is again used as active medium in the gaps. In total the hadronic calorimeter covers a pseudorapidity range of $|\eta| < 4.9$.

The resolution of the hadron calorimeter is worse than the resolution of the EM calorimeter and is expected to reach [40] typical values of about

$$\frac{\sigma(E)}{E} = \frac{60\%}{\sqrt{E}}\,[\text{GeV}]. \tag{3.6}$$

The missing transverse energy is expected to be measured with an accuracy of about

$$\sigma(E_T^{\text{miss}}) = (0.53 \text{ to } 0.57) \times \sqrt{\sum (E_T = 20 \text{ to } 2000\,\text{GeV})}. \tag{3.7}$$

3.3.3 Muon System

The muon detector system is responsible for the overall dimension of ATLAS. It is based on a combination of three air-core superconducting toroid magnet systems, two end-cap and one barrel toroid, that generate magnetic fields large enough to bend the muon tracks, that are the only charged particles that cross all the inner sections described above. The high field strength especially aimsw at muons with high p_T. The design goal is to measure muons with momenta up to 1 TeVwith a resolution below 10%. The barrel part covers a range $|\eta| < 1.4$ and is built of eight racetrack-shaped coils enclosed in vacuum vessels with 25.3 m length at a diameter of 20.1 m. The barrel field is designed to provide a bending power of 1.5 to 5.5 Tm. The end-cap toroids are likewise built out of eight coils each which are mounted together inside a large cryostat. They reach a bending power of 1 to 7.5 Tm in the covered region of $1.6 < |\eta| < 2.7$. The intermediate regions are covered by superpositions of both fields with less bending.

The precision momentum measurement of the bent muon tracks is accomplished by three cylindrical layers of chambers in the barrel region[7] and three layers of planar chambers installed in the end-cap regions perpendicular to the beam[8]. The cylindrical chambers are Monitored Drift Tubes (MDTs). The tubes have a diameter of 3 cm and are filled with 93% Ar and 7% CO_2 gas at 3 bar pressure. The muons passing through ionise the gas and the resulting electrons are collected on a tungsten-rhenium wire at high voltage. The MDTs will achieve a resolution of 60 to 80 µm. As planar chambers Cathode-Strip Chambers (CSCs) are used. CSCs are

[7]The MDTs are mounted on and between the toroid coils.
[8]The CSCs are mounted in front and the two end-cap toroid magnets.

multiwire proportional chambers that are separated by cathode plains orthogonal to the beam. They achieve a resolution of 40 µm in the bending plane and 5 mm in the transverse plane. The lower transverse resolution is caused by the position of the readout system. With the help of an optical alignment system and dedicated algorithms the position resolution of a muon track is reduced to 30 µm.

Additionally to the described momentum measurement system the detector also includes a muon trigger that covers a range of $|\eta| < 2.4$. The trigger identifies bunch-crossings, provides p_T thresholds and provides position information in the direction orthogonal to the that measured by the precision-tracking system.

The expected muon p_T resolution reaches 4% over a wide range of p_T (15-200 GeV/c) and differs over the η range varying between 3 and 4 % for $|\eta| < 1$ and about 9% at $|\eta| \approx 1.5$.

3.3.4 Trigger System

The LHC will collide bunches of particles every 25 ns. At the targeted maximum luminosity of $10^{34}\text{cm}^{-2}\ \text{s}^{-1}$ each bunch-crossing will contain an average of 23 inelastic pp collisions resulting in an event rate of up to 1 GHz. With an event size of approximately 1.3 Mbyte this would result in a data current of 1 PByte/s which is technically impossible to handle for a readout system. To circumvent this problem ATLAS integrated a three-level trigger system that reduces the data amount based on selection criteria and Regions-of-Interest (RoIs).

The Level 1 (L1) trigger looks for the following classes of particles: muons with high p_T, electrons, photons, jets and hadronically decaying tau leptons. In addition it searches for events with large missing energy and high transverse energy. Areas with such signatures are marked as RoIs. To accomplish a short latency below 2.5 µs, the L1 trigger is implemented as electric circuits into the detector and thus not easily reconfigurable. The events marked correspond to a reduction of the initial event rate down to 75 kHz.

The RoI information from the L1 trigger is handed to the Level 2 (L2) trigger which uses increased granularity and precision to reduce the event rate down to 3.5 kHz. Each event takes roughly 40 ms to process. L2 decisions are finally passed to the Event Filter which performs a final selection and triggers the readout with a rate of 200 Hz. L2 and Event Filter form together the High-Level Trigger (HLT) which is fully implemented in software and thus allows later adaptation to analysis needs. The final data rate which is passed to the storage system is estimated to reach about 300 Mbyte/s with peak rates of 600 Mbyte/s, which is still demanding for the follow-up storage systems.

Chapter 4

Analysis Tools and Data Models

In the preparation of this study a group initiative has been started to create a tool for easy data access to the ATLAS data files. The tool is supposed to convert the data into smaller and more easily accessible data files. One main goal was also that the tool shall be usable in all environments supporting the ATLAS software framework Athena, namely local installations as well as computing grid sites. To underline the demand and basic functionality of this tool, a short introduction into the ATLAS computing model will be given. After that, the tool will be described shortly and the analysis flow used in this study will be outlined.

4.1 ATLAS Analysis Infrastructure

As outlined in Section 3.3.4 the raw data produced by the ATLAS detector will put high demands on the computing infrastructure of the collaboration. This makes an analysis task more challenging than for older experiments with centrally stored raw data. The ATLAS Collaboration has developed several systems that helps to fulfil these demands and to provide the analysers with the needed data:

- in cooperation with other LHC experiments a worldwide distributed analysis network has been installed: the LHC Computing Grid (LCG);
- in the ATLAS Computing Model common data file structures have been defined;
- the ATLAS Event Data Model (EDM) has been developed to ensure unified interfaces and data objects through the full processing chain;
- a common software framework (Athena), which includes both online and offline process software, has been built.

ATLAS Distributed Analysis In the large collaborations of the LHC experiments, data has to be made available to all groups worldwide involved in analysis and data processing. A central computing centre would not suffice to achieve this goal while at the same time offering enough computing power to run analysis tasks. Instead a computing grid has been set up which distributes the data to local sites that offer CPU power for user tasks. The main concept is to enable the grid users to send analysis jobs to the data storing sites. The grid has the layout of a tree and separates the computing sites into several layers based on their resources. The layers are named tiers and numbered from zero to three. There is only one Tier0 site based at CERN which receives the raw data, stores it and passes it to the next layer. Processing of raw data into other formats is also accomplished at the Tier0 site. Several Tier1 sites help process the raw data and offer storage for their geographic region. Tier2 and Tier3 sites are the main user analysis sites and are also responsible for performing Monte Carlo production.

ATLAS Computing Model The amount of raw data is too large to distribute it to every user. To reduce the data size without removing needed data, two main file formats have been established: Event Summary Data (ESD) and Analysis Object Data (AOD). ESD files are generated directly from raw data. These files contain detailed information to allow algorithms to perform particle identification, energy calibrations, track studies etc. These files are mainly used by the performance groups and for alignment as well as detector testing tasks. The target size of ESDs is set to 500kB per event.

AOD files are aimed at analysis groups and contain already reconstructed physics objects. Performance groups were established within the collaboration to investigate the best ways of reconstructing the different physics objects (electrons/photons, muons, jets, etc.) and building reconstruction tools for general application. The common definition of physics objects ensures an easy comparison between analyses. Various quality parameters are stored in the files and can be applied by the user. The size of the AOD files is aimed at 100kB per event allowing wide distribution over the grid sites and easier data handling.

There are still plans to break the AOD files further down into different files for the various physics groups. This file format is called Derived Physics Data (DPD) and is currently in the process of definition in the different physics groups. All the above mentioned file formats are based on the POOL persistency framework [41]. It ensures easy access in the grid structure over a database catalogue. As such it is possible to address objects without a dependence on the underlying storage technology. While this has vast advantages in grid analyses the abstract handling of these objects is not very convenient in local data access on the single files.

Athena Software Framework The Athena framework is a big collection of software used in all parts of the ATLAS experiment's data analysis and processing. It

offers a common base for both online and offline reconstruction of raw data, is used for Monte Carlo production and contains a lot of tools for very different purposes. Additionally it is possible to use the framework to access data and to perform analysis tasks. The Athena framework is based on compiled C/C++ code and uses Python as a scripting language at execution time. It is based on the Gaudi software initially developed for the LHCb project. The framework is installed on all ATLAS grid sites allowing job execution. It is constantly in development, especially to improve the reconstruction algorithms.

4.2 Ntuple Creation with Gardener

Most analyses, like the one described here, are based on the ROOT data analysis framework [42] which offers a fast way to process a large amount of data and is well documented making it easy for beginners. The described AOD files cannot be directly accessed by ROOT macros without the Athena framework as an additional layer. Another problem of running analysis jobs on remote sites is the time to process the data. It is not suitable to perform small changes of the code for testing purposes and the compilation and linking of the Athena libraries consume additional time. To circumvent these problems it was decided to create an Athena-based tool that could run on remote sites as well as in local environments and process the needed AOD content into a plain ROOT tree.

Based on this basic functionality the project was named Gardener indicating the cutting of not needed data and growing a new tree with just used variables. The package follows the general guidelines for ATLAS software and has a structure similar to other Athena modules as indicated in Figure 4.1. The gardener and src directories contain the main C++ code of the package. A template is offered to produce new modules. The requirements file is used to pass the dependencies on other packages to the Athena framework. The share folder offers Python scripts for definition of input files and the Athena specific job options file allows to change cut variables and data container names without recompiling the full package.

Over time the package has been extended with core functionality to process important physics objects like electrons, muons, jets, photons and the missing transverse energy. Another module used in this study allows truth information in the AOD to be accessed. Modules have also been included for very specific analyses which will not be detailed here. The package also performs preselection by applying cuts and requiring certain quality parameters. The cut variables can be adjusted by the user in the job options. This is specially useful to produce analysis-specific output files with minimal size.

The first version of Gardener was based on Athena version 13.0.40. As some samples were only available from the big production in Athena version 12, it was necessary to backport the package to this old release. Support for newer releases of Athena is continuously added so that Gardener runs on the most recent releases 14.2.X, 14.5.X

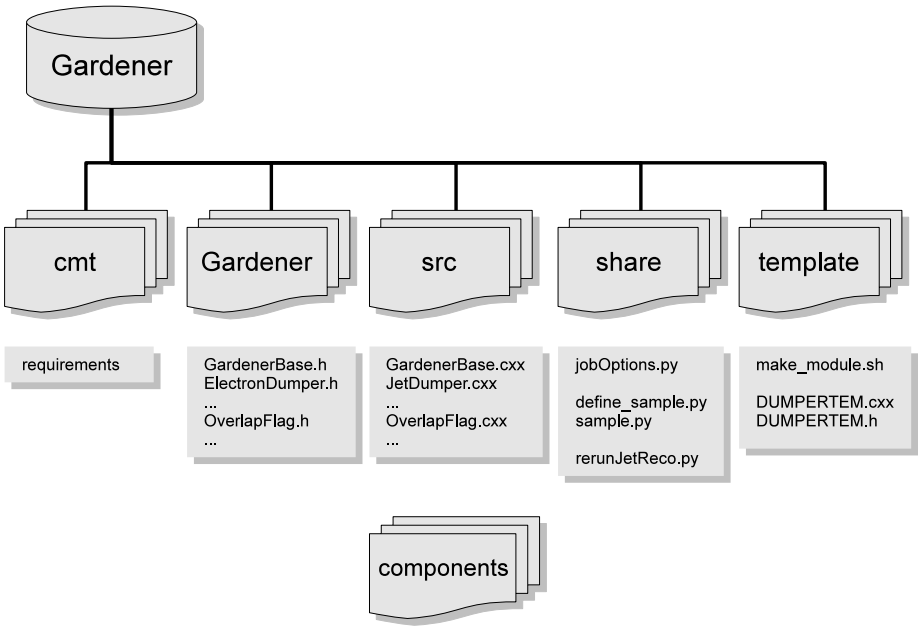

Figure 4.1: Structure of the Gardener software package.

and 15.0.X. Recently the package received a whole new structure making more use of the functions defined in the EDM. The goal here is to make Gardener a software package that can be verified by conveners in case of starting a publication process. It will be possible to include the full analysis code directly into the Gardener package without the intermediate step of data reprocessing. As such, the package can be uploaded to a central repository and be validated by the publication board which complies with the official ATLAS publication guidelines.

In summary a very useful tool has been created using understandable source code. It fully applies the guidelines of the ATLAS EDM, supports the distributed analysis model, can be extended in a modular way and offers easy access to the AOD and ESD data structures. It can optionally create flat ROOT ntuples and also contain full analysis code for publication submission.

4.3 Data Analysis Flow

A short overview shall be given here about the tools used for this analysis. As a first step, the Gardener tool was adapted to the selection criteria described in Chapter 6 and to run on the AOD data samples described in Section 5.4. The package was then submitted to the computing grid to create flat ROOT ntuples for further fast

analysis.

The tool SFrame [43] was used to reprocess the created ROOT files. Within the tool the final selection of objects has been done and control histograms were created. At the same time the necessary variables like mean and medians were calculated. The output is again stored in a ROOT file. After this process only one ROOT file for each sample is left and it possible to conduct all further analysis steps on these files using small ROOT scripts. Theses tasks include histogram and graph creation, calculation of derived variables and the setting of the final output design and content of plots.

This workflow offers a very high flexibility and fast processing time. The application of SFrame sets low entry barriers for newcomers as it executes most data management tasks in an easier way than ROOT and reaches a very high speed looping over the available events in the different data files. It is therefore highly recommended as a tool for newcomers.

Chapter 5

Monte Carlo Simulation

The presented study is based on predictions derived from Monte Carlo simulations that are applied to the data measured by the ATLAS detector. As the LHC accelerator has not yet started to produce collisions, only the prediction is studied here. The process of Monte Carlo generation for the used data sets will be explained in the following section.

The overall workflow of generating events that show the ATLAS detector response is split into several intermediate steps. First of all events of the considered process have to be generated taking the Feynman graphs of the process into account. Secondly a detector simulation calculates where the particles cross the different layers of the detector based on its geometry. Afterwards the response of the ATLAS detector is evaluated. The last step is the offline reconstruction of the detector data. The outcoming reconstructed data can then be used in analyses. Figure 5.1 shows the procedure of ATLAS event generation and simulation described below.

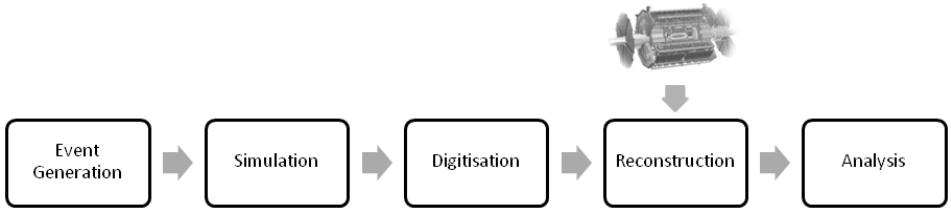

Figure 5.1: Flowchart of the Monte Carlo production chain.

5.1 Event Generation

A big selection of available Monte Carlo generators has been incorporated into the ATLAS software framework called Athena [44]. This way a convenient data flow

is ensured between all processes making it easy for the user to generate events and produce final events reflecting the response of the detector. The Monte Carlo generator is the first step in production and generates the events for a given process. In this study $t\bar{t}$ decays are analysed. The $t\bar{t}$ production process is calculated by the MC@NLO Monte Carlo generator [45] which includes next-to-leading-order processes.

The results of MC@NLO are passed as input to the HERWIG Monte Carlo package [46]. HERWIG generates radiation corrections[1], the decay of the top quark pair and the later hadronisation process of quarks. It uses additional modules for certain special tasks. A very important add-on for high-energy hadron colliders is the JIMMY generator [47] for multiple parton scattering. These multiple interactions are predicted to be a significant background in ATLAS events and are also called underlying events. An important module is also PHOTOS[48] which handles QED bremsstrahlung corrections in the cascade decays. To handle decays of tau leptons correctly, the TAUOLA[48] program is used.

The full generation as described above is controlled by the HERWIG package. The output of Monte Carlo generators consists of four-vectors for every particle which are handed to the Athena framework that stores the information into a data file. The events from the generator are referred to as truth as they contain the pure event without any detector impact. It is a valuable source for later cross-checks of selections and analysis results.

An important feature of the output of MC@NLO and other NLO generators are weighted events. Every generated MC@NLO event possesses an event weight which can be +1 or -1. The negative weighted events have to be subtracted from any distribution to make it accurate. This fact of course reduces the statistics of the samples and complicate certain analysis methods like the one shown in this study. It is though not allowed to ignore the weights as cross-sections and other variables will be inaccurate.

5.2 Full Detector Simulation

After finishing the Monte Carlo simulation of the events and their decays, the four-vectors of all particles are passed to the detector simulation. GEANT4 [49, 50] is used to simulate the passage of the generated particles through the ATLAS detector. It generates GEANT4 hits that contain information about the position of the particles that cross the detector and the energy deposit in the various components. A detailed geometry configuration file provides the ATLAS detector description and ensures a high accuracy of the simulation process. Due to the high number of particles in hadron collision events and the complexity of the detector, the simulation

[1] Initial State Radiation (ISR) and Final State Radiation (FSR)

process consumes time and resources. A faster and in some parts less accurate simulation process was developed to circumvent these limitations and allow higher event statistics. This process is described in more detail below.

After the simulation of the detector response, Athena initiates two more steps before producing the final output. The first process is called digitisation. It converts the GEANT4 Hits from the simulation process into physical detector responses like times and voltages. The result has the same structure and content as raw data delivered directly from the detector. Only triggers are not applied on this data yet while the built-in detector triggers of course affect the real data measured by ATLAS.

The last process is the reconstruction of the raw data into tracks and deposited energies. This process is the same for generated and real data and allows the analyser to compare them directly.

5.3 Fast Detector Simulation

Due to the long processing time explained above, the ATLAS Collaboration has also developed a faster simulation of the detector response. The corresponding tool is named Atlfast and available in two different version. Atlfast[51] was first implemented by just smearing the truth events with resolutions that were previously measured in fully simulated events. Atlfast events are generated with four to five orders of magnitude higher speed compared to events generated with the full detector simulation.

Atlfast II [52] is the current next generation of this approach. Instead of smearing the truth events it only changes parts of the simulation chain. The advantage is an identical reconstruction applied and the same structure of output files. It is also a more accurate method that generates events close to the fully simulated results. Atlfast II uses the full GEANT4 simulation for the inner detector. The calorimeter is simulated using FastCaloSim, which is a fast simulation that ensures the information to be reconstructed in the normal chain. Full simulation is applied to muons for all parts of the detector allowing matching of tracks from the inner detector and muon system. The current speed is still higher than the speed of full simulations and as such it is well suited to produce larger samples and for fast changes.

5.4 Data Sets

The data sets used for this analysis were produced centrally by the ATLAS Top Working Group. In total, five different sets with different top quark mass were used. Only the dileptonic and lepton+jets decay channels are included for all three lepton types. Full-hadronic decays were not simulated. Four samples contain a maximum of 60 000 events each for the top quark masses M_t = 160, 170, 180 and 190 GeV/c^2. One sample with high statistics was available close to the current world

average top quark mass ($M_t = 172.5$ GeV/c^2) with a total of 500 000 events. The samples were all produced with the event generation tools as explained above and simulated with Atlfast II. The production was done using Athena version 14.2.20 and as geometry the version ATLAS-GEO-02-01-00 has been passed to GEANT4. The collision energy is fixed to 10 TeV as this is the aim of the first running period.

The number of weighted events and the integrated luminosity for each data set have been calculated and are given in Table 5.1 below. Due to the falling production

M_t [GeV/c^2]	Data Sample	Events	Weighted	σ [pb]	$\int \mathcal{L} dt$ [pb^{-1}]
160.0	106203	59 150	43 476	313	138
170.0	106201	58 940	43 506	233	186
172.5	105200	496 260	365 942	217	1685
180.0	106202	59 796	44 158	176	249
190.0	106204	59 546	44 442	135	328

Table 5.1: Details about the used data samples. Weighted denotes the number of events after taking the MC@NLO weights into account. The integrated luminosity takes the weighted events into account.

cross-sections of $t\bar{t}$ for increasing top quark masses the integrated luminosity rises with the mass for the same number of events. The first running period is planned to produce about 200 pb^{-1} of data which roughly corresponds to the samples with low statistics.

The used samples only represent the signal channel while in real data also background is included. Thus it is needed to also produce samples for the background processes which will be explained in Chapter 6. The cross sections given in Table 5.1 represent the full $t\bar{t}$ production cross section except for the case that both W bosons decay hadronically. The cross section for the signal process studied in this analysis will be smaller as only a subset of the possible leptonic decays is selected as described in the following chapter.

Chapter 6

Signal and Background Processes

For the top quark mass determination in this study the leptonic decay products of top-antitop quark pairs have to be identified and their transverse momentum has to be measured. As described in Section 2.2.4 the W bosons in the top quark decay chain can decay either leptonically or hadronically. The combinations of decays for each of the top quarks allows $t\bar{t}$ decays to be classified into three general categories: the dilepton channel, where both W bosons decay leptonically, the lepton+jets channel, where one W boson decays leptonically and the other hadronically and the fully-hadronic channel, where both W bosons decay into quark-antiquark pairs. The combination of different lepton types, quark types and the three QCD colours allow 81 decay modes for $t\bar{t}$ pairs at lowest order. The resulting branching fractions are shown in Figure 6.1.

Cuts on a number of variables are used to select the different types of events and to separate them from background events with similar topologies. Such an approach is only feasible for two channels of the mentioned $t\bar{t}$ decays, namely the dileptonic and the lepton+jets channel. The fully-hadronic channel leaves only jets as reconstructable objects in the detector making it challenging to reduce its background considerably by just applying selection cuts. Therefore it is not further looked at in this study.

Additionally all $t\bar{t}$ events with τ leptons in their final states are not considered here. The ATLAS Collaboration has developed methods to identify τ lepton decays with hadronic products, as decay products from leptonically decaying taus cannot be separated from primary electrons or muons. These methods offer efficiencies around 30 % [40] and are thus not included in this analysis. As the products of τ leptons decaying leptonically cannot be separated from primary leptons they are taken into account if the event and the produced electrons and muons fulfil the selection criteria.

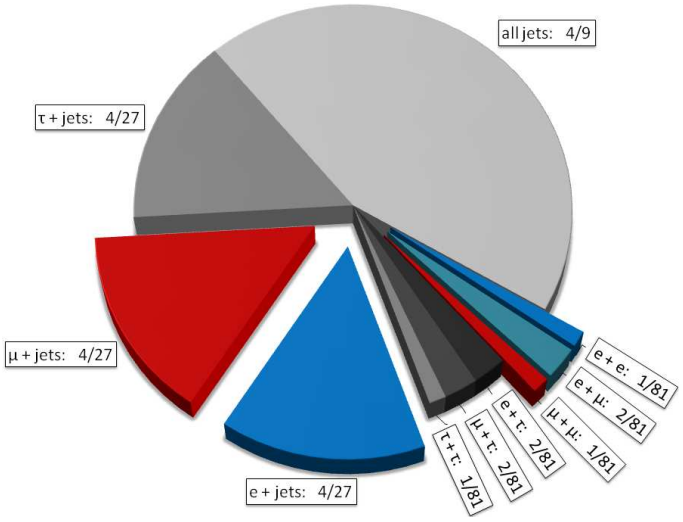

Figure 6.1: $t\bar{t}$ branching fractions.

6.1 Dileptonic Decay Selection

The selection of the dileptonic channel will be described in the following. The topology to be selected can be seen in the Feynman diagram in Figure 6.2. To select

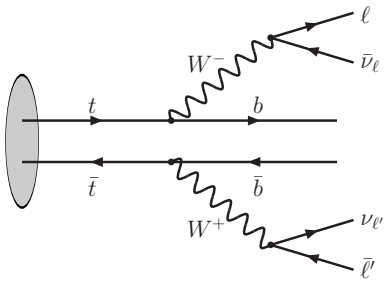

Figure 6.2: Feynman diagram of a dileptonic $t\bar{t}$ decay.

candidate events, the following requirements are made on every event:

- at least two reconstructed leptons with transverse momentum $p_T > 20$ GeV/c;
- missing transverse energy $E_T^{\text{miss}} > 30$ GeV.

The high missing transverse energy reflects the two neutrinos in the event that are not detected. The requirement for reconstructed leptons is based on the standard electron and muon definitions of the ATLAS Top Group [40]. Reconstructed electrons are particles that match the following specifications:

- the electron candidate has to pass a series of cuts based on shower shape properties in different compartments of the EM calorimeter;
- a track pointing from the ID to an energy cluster in the EM calorimeter;
- a veto on transverse energy in the tile calorimeter is applied based on the transverse energy of the EM cluster;
- energy in the EM Calorimeter has to match the momentum in the ID;
- tracks with low fraction of high-threshold TRT hits are rejected;
- the candidate has to be isolated: less than 6 GeV transverse energy are deposited in a cone $\Delta R = 0.2$;
- the candidate has to be in the pseudorapidity range of the ID: $|\eta| < 2.5$;
- candidates in a region with dead material in the EM Calorimeter are removed, $1.37 < |\eta| < 1.52$.

A muon in this analysis satisfies the following specifications:

- reconstructed candidates from MuonBoy [53] in the muon spectrometer;
- candidate tracks are matched to ID tracks using the STACO muon algorithm [53];
- extrapolated candidate tracks from MuonBoy have to match the interaction point;
- the candidate has to be isolated: less than 6 GeV transverse energy are deposited in a cone of $\Delta R = 0.2$;
- the candidate has to be in the pseudorapidity range of the ID, $|\eta| < 2.5$.

All these selection cuts are applied on ATLAS data from the detector. The standard specifications are already used in the reconstruction process so that standard muons and electrons are available in the centrally produced samples. Only some of the additional quality cuts have to be applied in the analysis. The aim of the quality cuts in this study is to produce a clean sample. Selection efficiencies are not so important as only dependencies and no absolute values are used to measure the top quark mass.

Another constraint is added after the event preselection as described above matching two oppositely charged leptons. This has not been implemented here as a distinct cut but a more sophisticated algorithm has been used to preserve higher statistics. The following procedure has been applied:

1. select the lepton with highest p_T in the event;

2. search for the lepton with next highest p_T and opposite charge;

3. mark the two leptons as the $t\bar{t}$ decay products.

The missing transverse energy is calculated using several different measured physical objects and as such is a potential origin for systematic errors. In this study the missing transverse energy with refined calibration is used. It is based on the calorimeter cell information for each reconstructed physics object in the event.

To create a very clean dileptonic decay sample, it can be useful to also require b-tagged jets in each event. As the b-tagging algorithms are still in a early stage of their development and a cross check with data cannot be done so far, this requirement is left out in this study. This can of course allow higher background influence and should be studied additionally.

Another possible cut to suppress background in the decays to ee and $\mu\mu$ combinations is to apply a Z boson mass veto, rejecting all events where the two-lepton invariant mass is in a range around the rest mass of the Z boson of 91.2 GeV/c^2[16].

6.2 Selection of Decays into Lepton and Jets

$t\bar{t}$ pairs decaying into a lepton and jets have a very different event topology compared to dileptonic $t\bar{t}$ decays. The Feynman graph for this decay channel is illustrated in Figure 6.3.

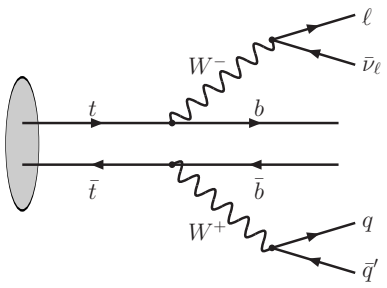

Figure 6.3: Feynman diagram of a $t\bar{t}$ decay into a lepton and jets.

The default ATLAS Top Group selection for this channel requires the following cuts:

- missing transverse energy $E_T^{\text{miss}} > 20$ GeV;
- only one reconstructed electron or muon with $p_T > 20$ GeV/c;
- at least four jets with $p_T^j > 20$ GeV/c, of which at least three jets have $p_T^j > 40$ GeV/c.

The lepton and missing transverse energy definitions have already been given above. The method applied to reconstruct jets is a seeded cone algorithm [40] with a cone radius of $\Delta R = 0.4$. It defines the jets using calibrated calorimeter tower signals. There are currently multiple jet reconstruction algorithms in use. The one used in this is the currently recommended one. More sophisticated methods are under consideration and in development.

6.3 Selection Cross-Checks

Before applying each method the selections described above have to be applied to the Monte Carlo samples covered in Section 5.4. To control the selection of the two different decay channels different cross-checks are made.

6.3.1 Dileptonic Decay Selection

The main cross-checks in the dileptonic channel target the lepton charges and their opposite charged combinations. After the main selection and before the matching of the charges is performed, the number of charged leptons per event is checked. An example for the $M_t = 180$ GeV/c^2 sample is given in Figure 6.4. The horizontal

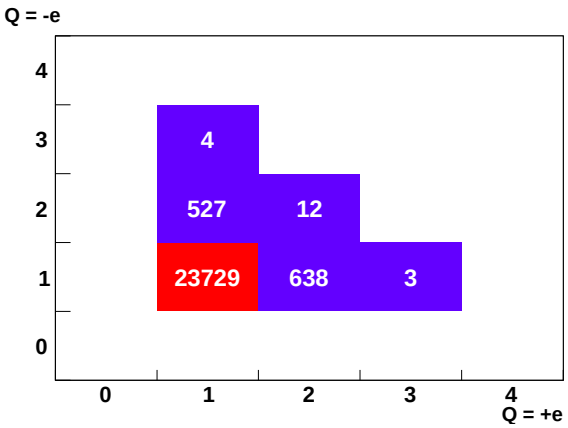

Figure 6.4: Number of negatively charged leptons over number of positively charged leptons per events after preselection for $M_t = 180\,\mathrm{GeV/c^2}$.

entries contain the number of positively charged leptons per event while in vertical direction, the number of negatively charged leptons is filled. Obviously most events already fulfil the requirement of two opposite charged leptons per event. An often applied cut would remove all events that contain more leptons from the sample. The more sophisticated matching of the highest p_T leptons applied here, includes those events.

After matching the opposite charged leptons the truth contents of these selected events is examined. The first aim was to check how many lepton+jets events with an additional high p_T lepton were picked up. In Figure 6.5 the truth content of selected events is shown. In truth only the leptons that are generated in the decay

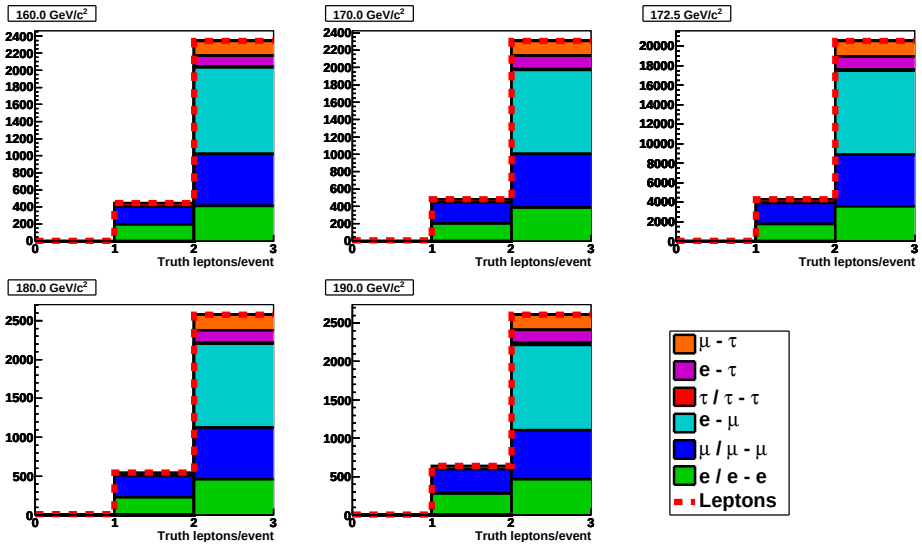

Figure 6.5: Truth leptonic top quark decay products inside the selected events for five different top quark masses. Bin one contains events with just one truth lepton originating from a top quark. Bin two contains the combinations of the two truth leptons for each event.

$t \rightarrow W \rightarrow \ell$ are inserted into the histogram. All the selected events that have only one truth lepton originating from that decay are lepton+jets events. This corresponds to about 16 % lepton+jets background events in the selection. These single lepton events are mainly composed of electrons and muons. Only a small amount of tau leptons are included which decay leptonically so that the resulting electron or muon is detected and selected.

The composition of events with two truth leptons is consistent with the expectation. Most events are composed of electrons and muons while around 10% contain tau leptons that again decay leptonically. It is also noticeable that only very few $\tau - \tau$ combinations are included. Two leptonically decaying taus in one event is suppressed. This can be explained with a leptonic branching fraction of 17.8% to electrons and 17.3 % to muons [16]. The doubled branching fraction of $e - \mu$ combinations with respect to same-lepton combinations is also visible.

To control the selected events also for misidentifications of leptons a direct cross-check of the reconstructed and truth leptonic event content is helpful as shown in Figure 6.6. The diagonal elements in the red enclosure show that the majority of the events are selected correctly compared to their truth content. Only small deviations are present where an electron is misidentified as a muon and vice versa. This can be an effect of the charge combination algorithm. In general this never happens

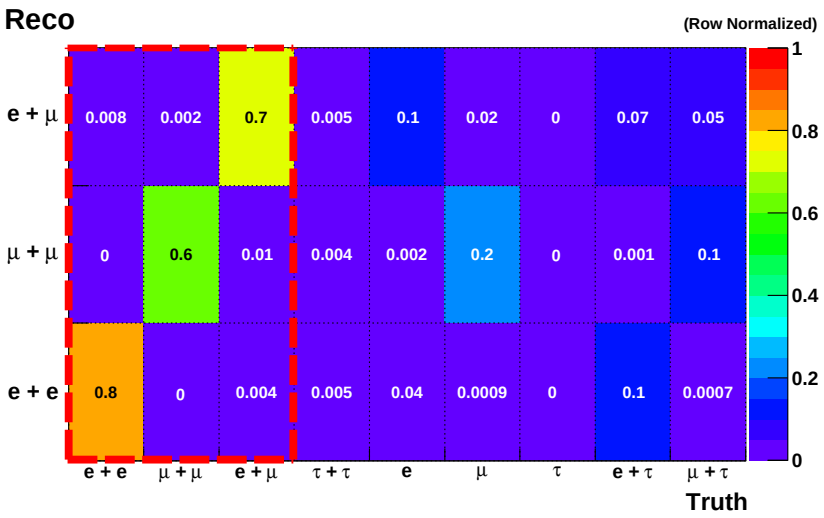

Figure 6.6: Selected lepton combinations over truth lepton combinations for the sample $M_t = 172.5$ GeV/c^2.

for both leptons at the same time. The wrongly selected single-lepton events can again be seen in this representation as well as tau leptons where the decay product is reconstructed.

The results of the selection together with the selection efficiencies are summarised in Table 6.1. The selection efficiency given in the table is the number of selected events in the sample divided by the number of dileptonic $t\bar{t}$ decays calculated from the branching fraction of dileptonic decays with electrons or muons from the W decay. The above described background of lepton+jets events and events with taus is still included enhancing the efficiency. It has also to be taken into account that the sample does not contain any full-hadronic decays and that only electrons and muons are selected. The efficiency increases with rising top quark mass. With a higher top quark mass, the p_T distributions are generally shifted towards higher values increasing the selection efficiency.

M_t [GeV/c^2]	Weighted Events	Selected	Efficiency
160.0	43 476	2 039	54.2 %
170.0	43 506	2 118	54.8 %
172.5	365 942	18 497	56.9 %
180.0	44 158	2 381	60.7 %
190.0	44 442	2 478	62.7 %

Table 6.1: Selection results for dileptonic $t\bar{t}$ decay channel.

In Figures 6.7 and 6.8 control plots for standard η, ϕ and p_T distributions are shown for leptons after the selection. The ϕ distribution shows the expected flat shape over the full range of $-\pi$ to π. The η distribution falls down from the maximum at

the central region. The distribution is cut for $|\eta| < 2.5$ so that only leptons in the most sensitive regions of the detector are accepted. The distribution of lepton p_T is steeply falling from the cut at $p_T = 20\,\mathrm{GeV/c}$ that is marked in the plot.

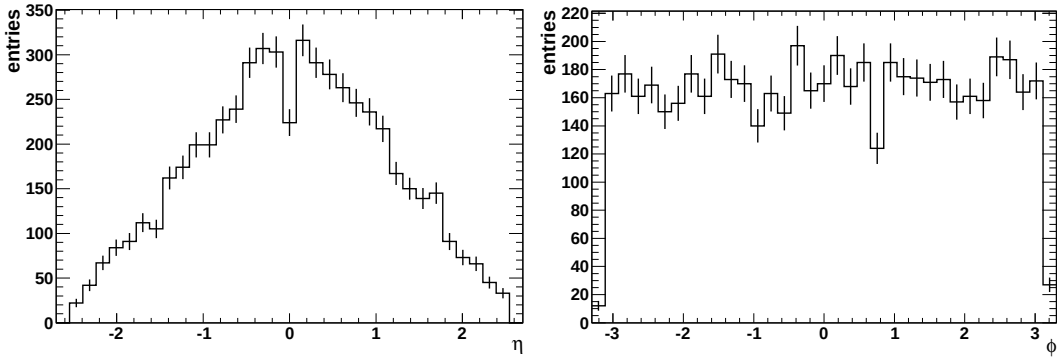

Figure 6.7: Distributions of lepton η (left) and ϕ (right) in dileptonic $t\bar{t}$ decays for $M_t = 170\,\mathrm{GeV/c^2}$.

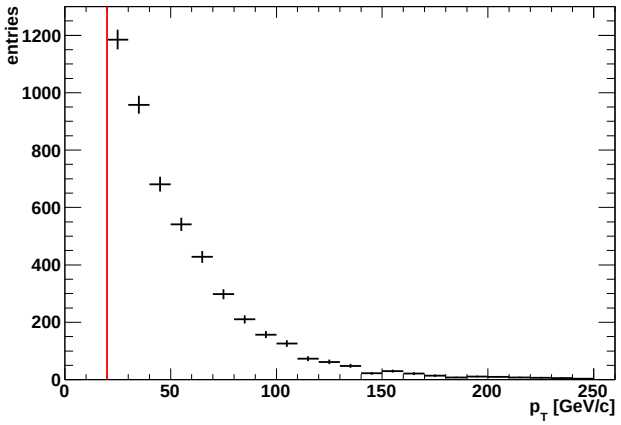

Figure 6.8: Distribution of lepton p_T in dileptonic $t\bar{t}$ decays for $M_t = 170\,\mathrm{GeV/c^2}$. The $p_T > 20\,\mathrm{GeV/c}$ cut is indicated by the vertical line.

6.3.2 Lepton + Jets Selection

In case of $t\bar{t}$ decays into one lepton and jets the jets deliver an interesting field for cross-checks. Many methods reconstruct the hadronic part of the decay as all its decay products are measured in the detector. The top quark mass can then be fitted on the combination of jets that result from the hadronic top quark. The appropriate distributions have been used here to check for inconsistencies in the selected events. To find the 2-jet combination resulting from the W decay a histogram has been filled with the invariant mass of all available 2-jet combinations in an event. The

result can be seen in Figure 6.9. The distribution peaks close to the current world

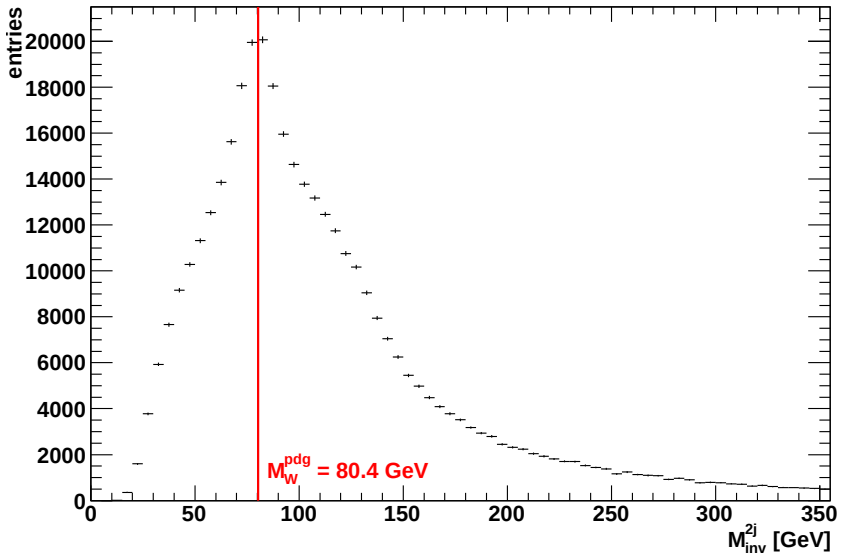

Figure 6.9: Invariant mass of 2-jet combinations in $M_t = 172.5$ GeV/c^2 sample. Marker for position of world average W mass.

average W mass of 80.4 GeV/c^2[16]. Suppression of wrong jet-combinations with a W mass cut has not been applied here in order not to lower the selection efficiency. This is also not needed as this study does not rely on the reconstruction of the hadronic part of the event and uses it just for selection purposes. Nevertheless it is worthwhile to investigate the further reconstruction of top quark candidates by calculating the invariant mass of the 3-jet combination with the highest combined p_T as shown in Figure 6.10. The idea is to select exactly the three jets from the hadronic top quark decay that point into a similar direction. Wrong combinations are found in the tail of the distribution and additionally enhance the bin content in the peak range. This background is referred to as combinatorial background and represents a strong source of systematic errors for studies in the lepton+jets channel that rely on the reconstruction of the hadronic decay. The formerly mentioned W mass cut can help to reduce this background significantly, but also tends to distort the shape of the mass peak as the shape of the combinatorial background in the tail and signal regions are not totally consistent.

Both distributions show the expected and in other analyses shown shape [40]. The selection results of the complete lepton+jets channel selection are shown in Table 6.2. The number of selected events is generally higher due to the higher branching fraction into lepton+jets decay. The efficiencies are lower than in the dilepton channel, but show the same rising behaviour as the p_T distributions of jets are also pushed to higher values for rising top quark masses.

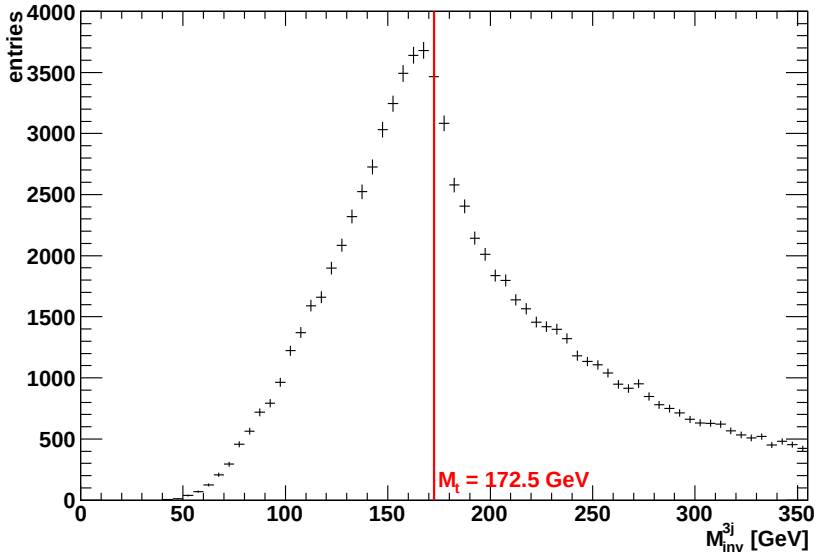

Figure 6.10: Invariant mass of 3-jet combination with highest p_T in $M_t = 172.5$ GeV/c^2 sample. Marker for position of top quark mass value of sample.

M_t [GeV/c^2]	Weighted Events	Selected	Efficiency
160.0	43 476	9 903	42.7 %
170.0	43 506	11 119	47.9 %
172.5	365 942	95 442	48.9 %
180.0	44 158	12 265	52.1 %
190.0	44 442	13 346	56.3 %

Table 6.2: Selection results for lepton+jets $t\bar{t}$ decay channel.

6.4 Main Background Processes

As explained above, background processes can have a similar event topology as the considered signal channels and thus are a source for systematic uncertainties in the analysis. Background events are suppressed in the signal event selection by applying selection cuts. While the cuts work very efficiently on some background channels, others will stay in the selected data. In the latter case it is important to estimate the background in other ways.

Potential background sources can be events with the same final-state particles registered in the detector or events with similar topologies and misidentified particles. The main sources for background for the $t\bar{t}$ decays are the following:

- W + jets
- Z + jets
- Single top
- $Wb\bar{b}$
- WZ
- ZZ
- WW
- $Wc\bar{c}$

From this list the W + jets contribution is expected to dominate. Studies of the background are not part of this analysis. Reliable background estimation is only possible once ATLAS produces data and inclusive Monte Carlo samples become available. To apply the methods discussed in Chapter 7 do not directly use selection efficiencies in the top quark mass calculation but depend on a clean selection of the decay channel. An estimation of the selection quality with the applied standard ATLAS selection can be found in [40]. The impact of non-suppressed background on the systematic error has to be studied once the method is applied.

Chapter 7

Top Quark Mass from Leptonic Decay Products

The aim of this study is the measurement of the top quark mass using information from the leptonic decay products resulting from $t\bar{t}$ decays in the dileptonic and lepton+jets channels. The method has been first proposed by Giokaris et al. in 2005 [54] and has successfully been applied to CDF data since [55, 56, 57]. A first internal note also describes the method for the lepton+jets channel only with the ATLAS detector [58].

The error on the current combined top quark mass measured at the Tevatron is mainly influenced by systematic uncertainties. The main sources of these systematic uncertainties are the error on the jet energy scale (JES) and errors from b-tagging. The JES is used to calibrate the absolute energy of jets measured by the detectors to its real value. A wrong JES can have a large impact on analyses that use fully reconstructed decays to derive the top quark properties. b-tagging refers to methods that tag b-jets, i.e. mark jets in the events that result from b quarks. Errors on these methods lead to lower efficiencies in the event selections and can also introduce wrongly combined jets in the event reconstruction. On longer running experiments the b-tagging efficiencies and the accuracy of the JES determination will of course improve as more data is available to calibrate the detector components. The current uncertainty on the top quark mass resulting from the JES is $\pm 0.73\,\mathrm{GeV/c^2}$ [20] at the Tevatron.

In the first running period of the LHC, both the JES and the b-tagging efficiencies will have large uncertainties, which will limit the precision of the top quark mass measurement using hadronic decays. Therefore methods are favoured that make less use of jet energies and b-tagging. The lepton transverse momentum (p_t) used in this study is a very good variable in this respect as it can be precisely calibrated with $Z \to \ell\ell$ decays by using the Z-boson mass which has been measured very accurately by the LEP experiments [1].

The initially cited studies have shown a linear dependence of $\langle p_T \rangle$ on the top quark mass over a wide range. Three different approaches were investigated to study this dependence in more detail:

- mean transverse momentum fit;
- median transverse momentum fit;
- fitting of transverse momentum spectra.

In the third method a fit is applied to the distribution for each top quark mass sample and the fitting results are combined afterwards to measure the top quark mass. The first two methods are very similar. The mean value and median value of the p_T distributions in selected events are calculated for each top quark mass Monte Carlo sample. The values are subsequently fit as a function of the top quark mass.

In the following, the three methods will be explained and their results shown. Additionally an outlook on the precision of the methods is given and the results are compared to each other.

7.1 Mean Transverse Momentum Fitting

The first method used in this study relies on the dependence of the mean transverse momentum of the electrons and muons, $\langle p_T \rangle$, on the top quark mass, M_t. The measurement is conducted in three steps:

1. calculate $\langle p_T \rangle$ for every available top quark mass sample;
2. fit $\langle p_T \rangle$ as a function of the top quark masses;
3. use the fitting results to calculate the top quark mass from data.

The parameters of the fit give a handle on the top quark mass and can be used to calculate it from the $\langle p_T \rangle$ of measured data.

7.1.1 Mean p_T Calculation

To make the calculation of mean lepton momenta as reliable as possible and to provide realistic errors to later estimate the method's precision, it is implemented directly into the processing stage after the event selection and not retrieved from histograms. As pointed out in Chapter 5.1 the event weights of MC@NLO have to be taken into account when calculating the variable and its error. Thus a weighted mean was used:

$$\langle p_T \rangle = \frac{\sum w_i \, p_{Ti}}{\sum w_i}, \tag{7.1}$$

where w_i are the event weights. It has to be summed over all leptons and not just the events as dileptonic decays contain two leptons. The error of each single $\langle p_T \rangle$ value is

$$\Delta p_{Ti} = \sqrt{V} = \sqrt{\frac{\sum w_i \left(p_{Ti} - \langle p_T \rangle\right)^2}{\sum w_i}} \tag{7.2}$$

where V stands for the variance. MC@NLO only uses weights of $w_i = \pm 1$ thus it is possible to convert the sum of weights to $\sum w_i = N_+ - N_-$ where $N_\pm$ are the total number of positive and negative weighted events or leptons. The error of the mean value is then calculated using Gaussian error propagation:

$$\Delta \langle p_T \rangle = \sqrt{\frac{N_+ + N_-}{(N_+ - N_-)^2} \left(\langle p_T^2 \rangle - \langle p_T \rangle^2\right)}. \tag{7.3}$$

The calculations for $\langle p_T \rangle$ are made for electrons and muons separately and for all leptons. This allows the impact of the two different lepton types on the overall value to be seen.

7.1.2 Top Quark Mass Dependence on the Mean Transverse Momentum

The results of the $\langle p_T \rangle$ calculations are shown as a function of the top quark mass used to generate the sample. Distributions for both, dileptonic and lepton+jets events, can be seen in Figure 7.1. The dileptonic channel generally has lower $\langle p_T \rangle$ val-

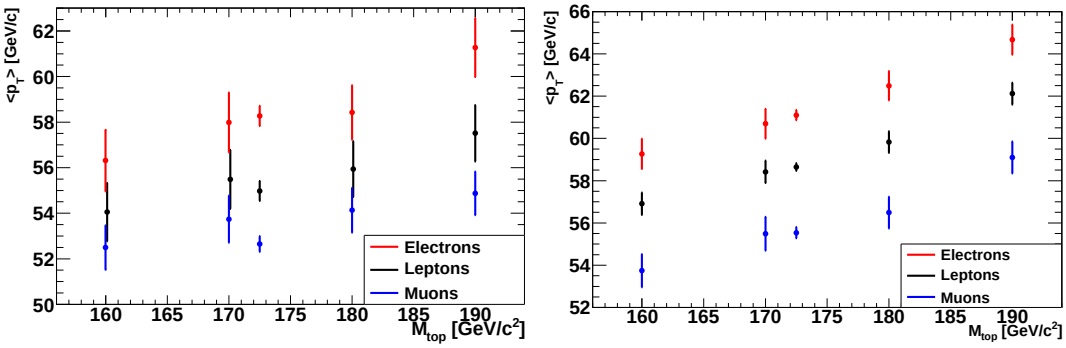

Figure 7.1: $\langle p_T \rangle$ over M_t in dileptonic (left) and lepton+jets (right) $t\bar{t}$ decays.

ues than the lepton + jets channel. Also the error bars are larger in the dileptonic case as the statistics is lower. The overall trend looks the same for both channels: electrons have a higher $\langle p_T \rangle$ than muons due to their different particle definitions. A linear trend is observed more distinctly in the lepton+jets case.

7.1.3 Fit $\langle p_T \rangle$ as Function of Top Quark Masses

With a linear fit of the produced distributions it is possible to get a handle on the top quark mass. Fitting a normal linear function to the data sets would result in two correlated fit parameters. This correlation makes the direct interpretation of the parameters hard. Thus it is helpful to decorrelate them by shifting the fit to the centre of gravity of the distribution. Here the fit is shifted to the centre of gravity of the lepton distribution to allow the easier comparison between the results for electrons, muons and the overall lepton fits. This leads to slightly higher errors in the electron and muon fits. The fit function is then:

$$\langle p_T^{\ell} \rangle = (M_t - m_0)\,\lambda + \kappa, \tag{7.4}$$

where λ is the slope and κ the intercept at the centre of gravity, m_0. The result of the fits are shown in Figures 7.2 and 7.3.

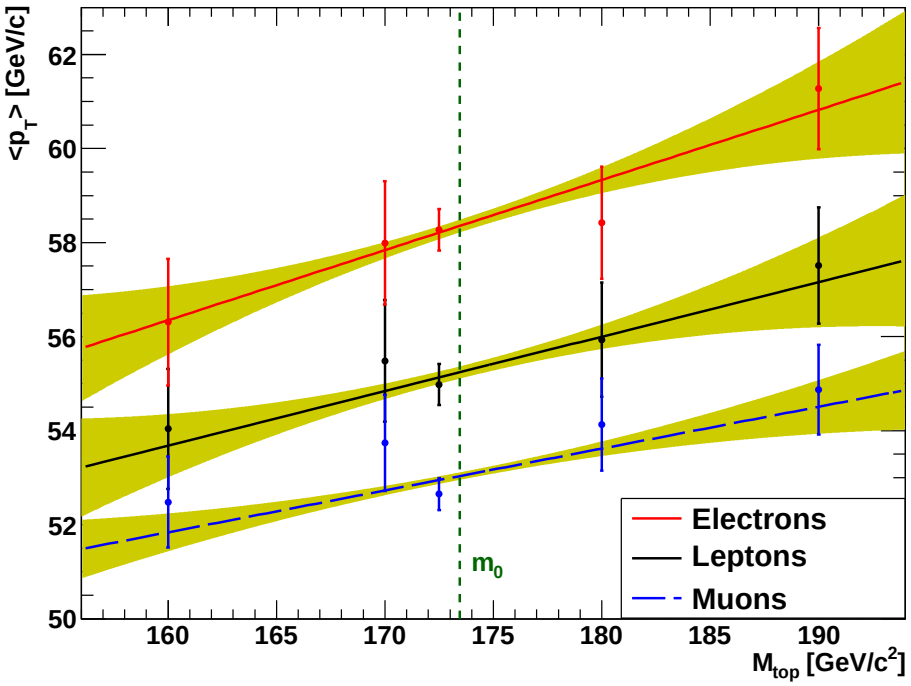

Figure 7.2: Fit of $\langle p_T \rangle$ for dileptonic $t\bar{t}$ decays for electrons and muons separately and the full lepton distribution. The dashed line shows the centre of gravity for the lepton distribution at $m_0 = 173.4\,\mathrm{GeV/c^2}$.

The error bands for the 1σ error on the fit are also plotted into the graphs. These errors are smallest in the region around the centre of gravity of the distribution also due to the sample with high statistics situated in that region. The results on the lepton+jets channel shows nicely the impact of higher statistics on the fit

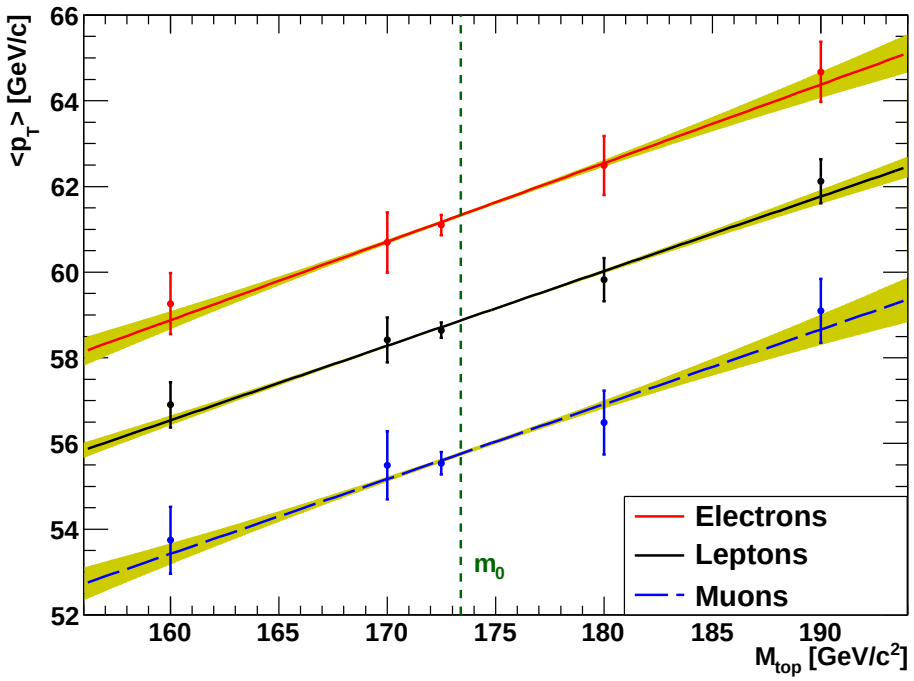

Figure 7.3: Fit of $\langle p_T \rangle$ for lepton+jets $t\bar{t}$ decays for electrons and muons separately and the full lepton distribution. The dashed line shows the centre of gravity for the lepton distribution at $m_0 = 173.4\,\mathrm{GeV/c^2}$.

quality compared to the dileptonic case. The numerical results of the fits are given in Table 7.1.

	Dilepton Channel		Lepton+Jets Channel	
	Slope (λ) [c]	Intercept (κ) [GeV/c^2]	Slope (λ) [c]	Intercept (κ) [GeV/c^2]
$\ell^{\pm}$	0.116 ± 0.055	55.24 ± 0.36	0.174 ± 0.023	58.87 ± 0.14
$e^{\pm}$	0.149 ± 0.057	58.35 ± 0.36	0.183 ± 0.031	61.33 ± 0.20
$\mu^{\pm}$	0.089 ± 0.042	53.04 ± 0.28	0.174 ± 0.033	55.76 ± 0.22

Table 7.1: Results of the $\langle p_T \rangle$ fits to electron, muon and combined samples.

The correlation coefficient of the two parameters is zero by construction. The slopes as well as the significance, meaning the value of the slope divided by its error, are generally higher for the lepton+jets case. The slopes of the fits for electrons, muons and leptons in this case are compatible within the errors. The dilepton channel shows a much higher variation of the slope for the different particle types due to low statistics. In general the lepton+jets channel is the better choice for this case if the purity of the sample is high enough. As the dilepton channel has a higher selection purity it is possible that the variances are compensated. A problem of the dileptonic

channel remains the lower statistics due to the lower branching fraction.

With the obtained fit parameters and their errors, it would be now possible to apply the method to measured data. The selection that was used for the Monte Carlo has to be applied on data sets coming from the ATLAS detector and $\langle p_T \rangle$ has to be calculated. With that value it is then possible to obtain the top quark mass directly using the function:

$$M_t = \frac{\langle p_T \rangle_{data} - \kappa}{\lambda} + m_0 \tag{7.5}$$

The precision of the top quark mass determination will depend on the uncertainty of the $\langle p_T \rangle$ extracted from data as well as the uncertainties on the fit parameters which is again dependent on the Monte Carlo precision. In the application the Monte Carlo statistics should be as high as possible to reduce the statistical error and to minimise the uncertainties due to the fit parameters. With large Monte Carlo samples it will be possible to extract the fit parameters λ and κ with high precision.

A variation of this method is to use the median value instead of the mean. This variation will be studied in the following Section. Afterwards the precision of both methods will be estimated and compared.

7.2 Median Transverse Momentum Fitting

In the transverse momentum spectrum shown in Figure 6.8 before a long tail at high p_T could be seen. The mean value is very sensitive to outliers in these tails. Single high p_T leptons thus have a high impact on the mean value. To overcome this problem a second variable is studied. The median value separates a distribution into halves. The upper half has values greater than the median, the lower half smaller values. To find the median value in a list, the list has to be sorted and the value in the middle of the distribution is the median. In case of an even number of weights, the mean value of the two median candidates is used.

As the used Monte Carlo samples for different top quark masses are generated with the MC@NLO generator, it is obligatory to take event weights into account. This makes the calculation of the median value and its errors more complicated as the median is not anymore just the middle member of the sorted list The approach taken here is to sort the list of leptons by their p_T value but at the same time preserving the event weight for every lepton. This way, the event weights get sorted simultaneously and can be used to find the median. The median is found by adding up the sorted event weights till one reaches half of the sum of all lepton event weights. The p_T of the corresponding lepton is then the median of the p_T distribution.

A similar problem arises when the error for the median value has to be calculated. In contrary to the mean value, it is not possible to just use a standard Gaussian error for the median. Instead the median has a defined standard error as follows

[59]:

$$\Delta\tilde{p}_T = (a-b)/\sqrt{12}. \tag{7.6}$$

The values a and b are equivalent to the value of the list member at the positions

$$\left(\frac{n}{2}+\frac{\sqrt{3n}}{2}\right) \text{ for } a \qquad \text{and} \qquad \left(\frac{n}{2}-\frac{\sqrt{3n}}{2}\right) \text{ for } b, \tag{7.7}$$

where n is the total sum of the weights of all leptons in the sample. As these positions can be real numbers, they are rounded to the next higher integer number. The calculated error is then symmetric. The Monte Carlo weights are taken into account in the same way as for the median itself. Again the weights are summed up until the weight reaches the above defined positions compared to the sum of weights for all leptons in the list.

Once the median value and its errors are calculated, they are also drawn as a function of the top quark mass of the according Monte Carlo sample. The linear dependence is again seen. The error bars are in general smaller than those of mean values. The distribution can then be fitted in the same way as for the mean values again shifting the fit to the centre of gravity of the distribution to remove the correlation between slope and axis intercept. The results of the fits an the 1σ error bands for the dileptonic and the lepton+jets channel are shown in Figures 7.4 and 7.5.

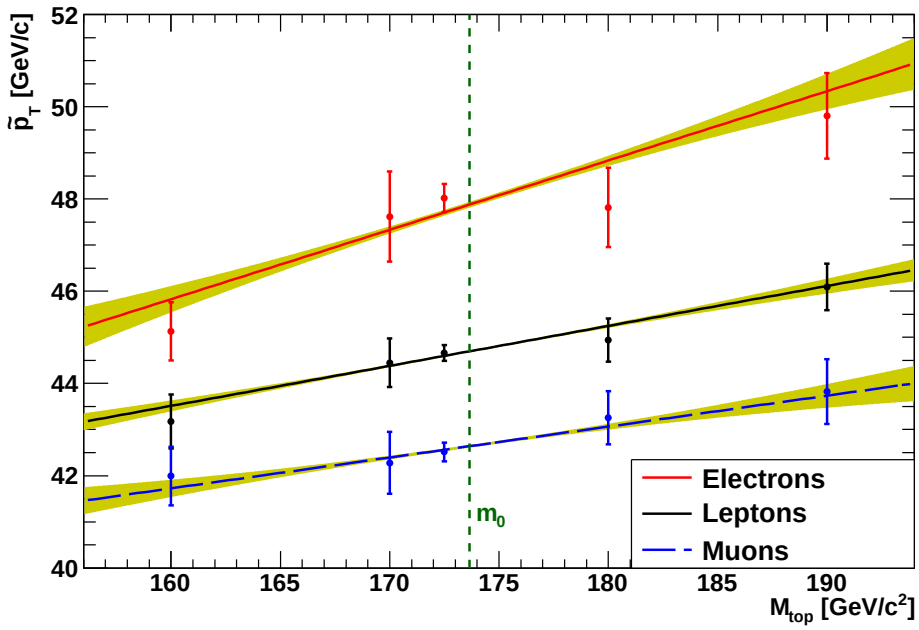

Figure 7.4: Fit of median p_T values for dileptonic $t\bar{t}$ decays for electrons and muons separately and the full lepton distribution. The dashed line shows the centre of gravity for the lepton distribution at $m_0 = 173.6\,\mathrm{GeV/c^2}$.

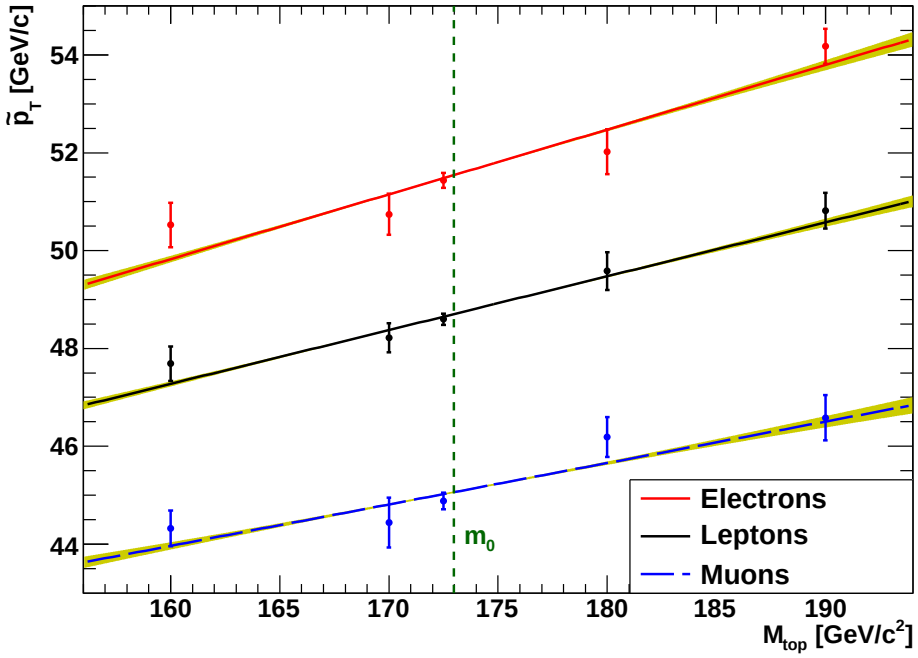

Figure 7.5: Fit of median p_T values for lepton+jets $t\bar{t}$ decays for electrons and muons separately and the full lepton distribution. The dashed line shows the centre of gravity for the lepton distribution at $m_0 = 173.0\,\mathrm{GeV/c^2}$.

The fit results for both channels are shown in Table 7.2. Qualitatively the results are the same as the results for the mean value. To make quantitative statements an estimation of the precision of the mass estimation has to be evaluated. This will be done in the next section together with a comparison of the two methods.

	Dilepton Channel		Lepton+Jets Channel	
	Slope (λ) [c]	Intercept (κ) [GeV/c^2]	Slope (λ) [c]	Intercept (κ) [GeV/c^2]
$\ell^{\pm}$	0.09 ± 0.02	44.69 ± 0.14	0.109 ± 0.016	48.70 ± 0.10
$e^{\pm}$	0.15 ± 0.03	47.88 ± 0.25	0.132 ± 0.017	51.54 ± 0.12
$\mu^{\pm}$	0.07 ± 0.03	42.64 ± 0.17	0.085 ± 0.018	45.06 ± 0.13

Table 7.2: Results of the median p_T fits to electron, muon and combined samples.

7.3 Comparison between Median and Mean

As there is no collision data available yet, it is only possible to make a rough estimation on the precision of this method. The calculations are the same for mean and medians. Exemplary it fill be shown for the mean values. The first step is to esti-

mate the error on a $\langle p_T \rangle$ determined from data. It can be achieved by extrapolation of the Monte Carlo error to the data:

$$\Delta \langle p_T \rangle_{\text{data}} = \sqrt{\frac{\sigma_{\text{mc}} \mathcal{L}_{\text{mc}} \epsilon_{\text{mc}}}{\sigma_{\text{data}} \mathcal{L}_{\text{data}} \epsilon_{\text{data}}}} \Delta \langle p_T \rangle_{\text{mc}} = \sqrt{\frac{\mathcal{L}_{\text{mc}}}{\mathcal{L}_{\text{data}}}} \Delta \langle p_T \rangle_{\text{mc}} \tag{7.8}$$

In this formula the cross sections, σ, and efficiencies, ϵ, cancel as they should be identical for data and Monte Carlo. What remains is a luminosity-weighting. Assuming a target integrated luminosity of 200 pb^{-1} for the first run of the LHC and using the high-statistics sample for $M_t = 172.5\,\text{GeV/c}^2$ and the lepton+jets selection the error would be $\Delta \langle p_T \rangle_{\text{data}} = 0.51\,\text{GeV/c}$ and $\Delta \tilde{p}_T = 0.33$ for the median. The second step is to propagate this error to an uncertainty on the mass measurement. This is again achieved with Gaussian error propagation:

$$\Delta M_t = \sqrt{\frac{(\Delta \langle p_T \rangle)^2}{\lambda^2} + \frac{(\Delta \kappa)^2}{\lambda^2} + \frac{|\langle p_T \rangle - \kappa|}{\lambda^4} (\Delta \lambda)^2} \tag{7.9}$$

This affirms the previous statement that the analysis is not based on cut efficiencies but rather depends on a clean sample. Only the relative luminosity is used here. In the later analysis the error on $\langle p_T \rangle_{\text{data}}$ and $\tilde{p}_T$ will be determined using the statistics of the data sample directly so that the luminosity of the Monte Carlo only affects the fit and the luminosity of data is directly reflected in the calculated top mass uncertainty. The estimated errors on a mass measurement using the mean value is

$$\begin{aligned} \Delta M_t &\approx 11.4\,\text{GeV/c}^2 && \text{for dileptonic decays and} \\ \Delta M_t &\approx 3.1\,\text{GeV/c}^2 && \text{for lepton+jets decays} \end{aligned}$$

For the median values, the same approximation gives

$$\begin{aligned} \Delta M_t &\approx 5.6\,\text{GeV/c}^2 && \text{for dileptonic decays and} \\ \Delta M_t &\approx 3.2\,\text{GeV/c}^2 && \text{for lepton+jets decays} \end{aligned}$$

The precision for both methods are the same for the lepton+jets channel. In the dileptonic channel however, where the statistics are lower, the median value achieves a considerably higher precision. Looking at the sensitivity of the two fit functions for dileptonic events, which is defined as the slope of the straight line fit divided by its error, it can be seen that the loss for the median value is smaller between the lepton+jets and dileptonic case. This could already be seen in the plots and corresponds to the expected behaviour for the median value as it is introduced to be less sensitive to single outliers in the spectrum. Especially for lower statistics in the Monte Carlo samples, the method seems to be more stable. It is also the better variable to apply to low data statistics at the beginning of the experiment based on the experiences of the fitting.

The errors in this estimation could be further reduced by generating more Monte Carlo events. The given error contains only statistical influences. A close analysis

of the systematic uncertainty is needed. Nevertheless the error is close to the uncertainty of the currently valid combined top quark mass measurements at Tevatron; thus demonstrating that the method is well worth pursuing further.

7.4 Transverse Momentum Spectrum Fitting

As a last approach a more complicated method was chosen to verify its adaptability to the ATLAS experiment. Instead of using only the information of a single parameter the whole p_T spectrum for each top quark mass sample is studied. Therefore the method will be more dependent on the theoretical uncertainty and the systematic description.

In the method the shape of the p_T distribution for each top quark mass sample is fit. The obtained fit parameters are then checked for their top quark mass dependence. The expectation given by the attempts at the Tevatron again showed a linear connection.

7.4.1 Description of Fit Function

The first task is to define a fit function that models the shape of the p_T distributions. An example for such a distribution is given in Figure 7.6 for the top quark

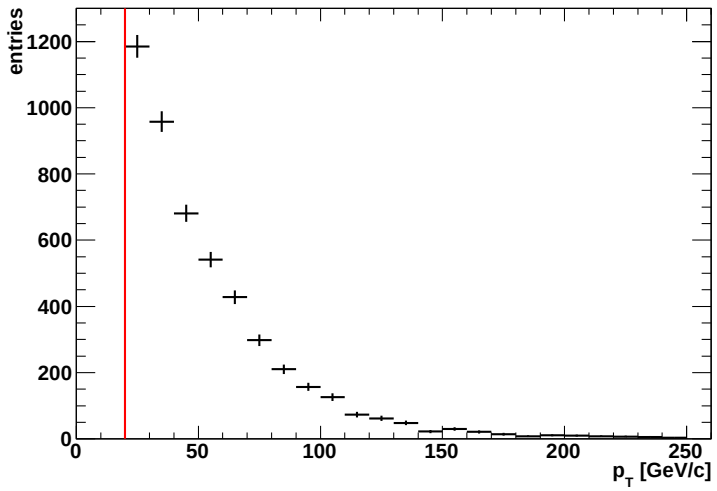

Figure 7.6: Lepton p_T distribution for $M_t = 170\,\mathrm{GeV/c^2}$. The vertical line illustrates the p_T selection cut at 20 GeV/c.

mass of $M_t = 170\,\mathrm{GeV/c^2}$. To model this distribution a superposition of a gamma

distribution and a Fermi function was proposed in [55]:

$$F(p_T) = \underbrace{\frac{1}{\Gamma(p+1, c/q)} \frac{1}{q} \left(\frac{p_T}{q}\right)^p \mathrm{e}^{-\frac{p_T}{q}}}_{\text{Gamma distribution}} \times \underbrace{\frac{1}{1+\mathrm{e}^{(c-p_T)/b}}}_{\text{Fermi function}} \tag{7.10}$$

The gamma distribution models the shape of the falling p_T distribution and the Fermi function describes the turn-on curve at the p_T cut. The function includes two constant parameters that are set to

$$c = 20 \text{ GeV/c} \qquad \text{and} \qquad b = 0.5 \text{ GeV/c} \tag{7.11}$$

These two constants define the Fermi function. Constant c sets the position of the Fermi-step and b sets its width. The gamma distribution is fitted by two variable parameters (p, q) to the shape of the spectrum.

First it is necessary to check how well the spectrum is described by the given function. Afterwards parameters have to be extracted that are sensitive to the top quark mass.

7.4.2 Fits in the Dileptonic Decay Channel

Before fitting each p_T spectrum, they were normalised to unity. This is helpful to see how well the function can discriminate between the different top quark mass samples. The fit was found to be very sensitive to the starting parameters. Suitable starting parameters for both channels are

$$p = 4.0 \qquad \text{and} \qquad q = 20.0. \tag{7.12}$$

The fit is applied to the weighted p_T spectrum using a minimum chi-square fit. The result of the application of the defined fit function to the dileptonic decay channel selection is shown in Figure 7.7. Visually the fit function describes the p_T spectra well with an average $\chi^2/ndof$ of 1.2. The numerical results of the fit function can be found in Table 7.3.

M_t	p			q			$\chi^2/ndof$	Correlation
160.0	0.084	$\pm$	0.097	31.5	$\pm$	1.6	0.8	6 %
170.0	0.208	$\pm$	0.100	30.6	$\pm$	1.6	1.4	7 %
172.5	0.161	$\pm$	0.032	31.5	$\pm$	0.5	2.2	6 %
180.0	0.273	$\pm$	0.084	30.3	$\pm$	1.2	1.0	7 %
190.0	0.165	$\pm$	0.080	33.7	$\pm$	1.4	0.6	6 %

Table 7.3: Fit results for the p_T spectrum of the dileptonic channel.

To extract the dependence of the two fitting parameters on the top quark mass, they are shown as a function of M_t in Figure 7.8. The parameters for each mass

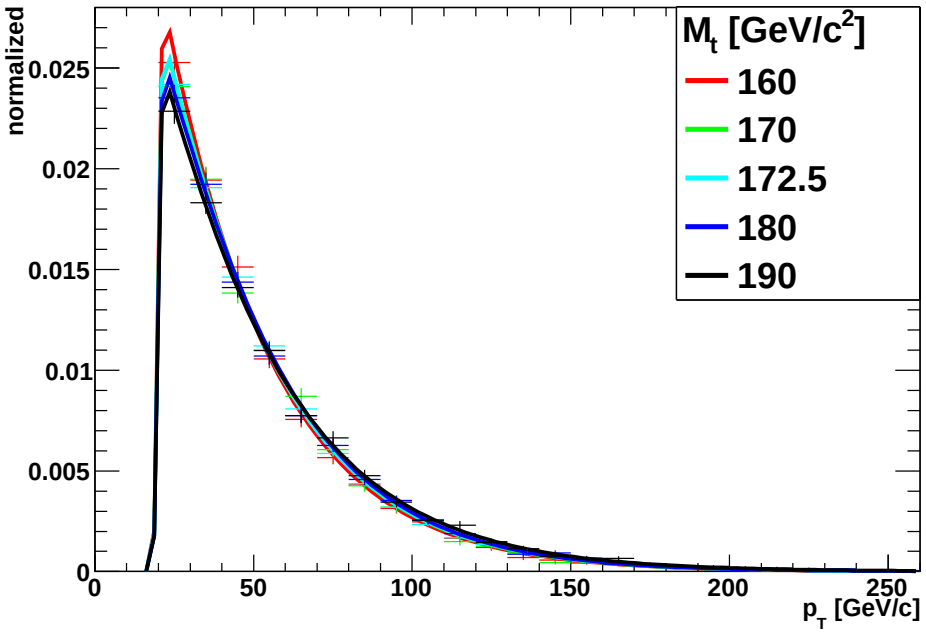

Figure 7.7: Fit of dilepton p_T spectrum with gamma $\times$ Fermi function.

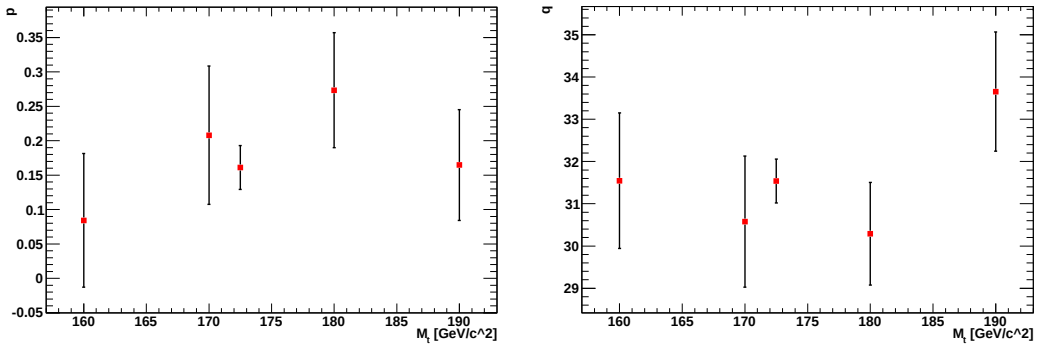

Figure 7.8: Fit parameters p (left) and q (right) of dilepton p_T spectrum fit.

are differing which shows a potential separation power of the chosen function. From the two plots for both fit parameters no obvious dependence can be inferred in this channel. This renders the method unsuitable for this channel with the available statistics.

7.4.3 Fits in the Lepton+Jets Decay Channel

The same fit function is applied for the lepton+jets decay channel. The result can be seen in Figure 7.9 with the numerical results in Table 7.4. There can be already seen

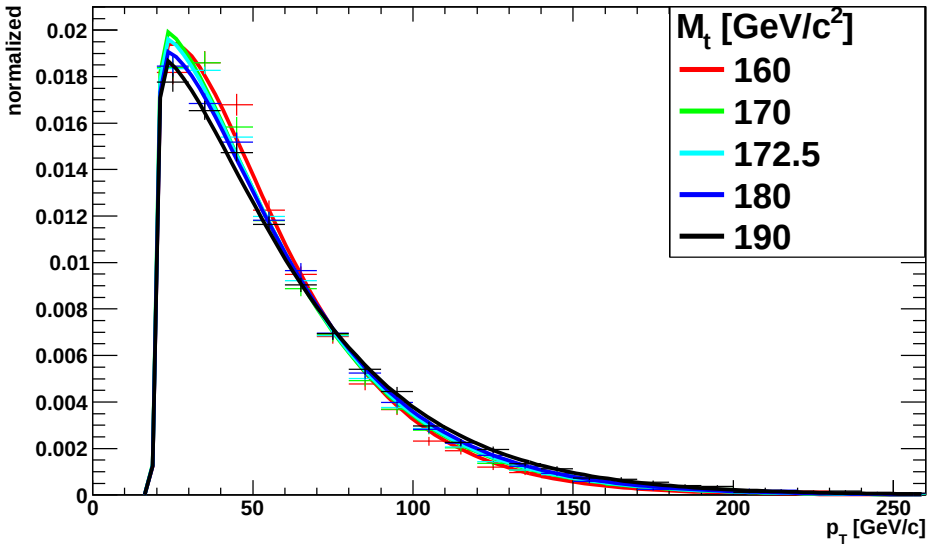

Figure 7.9: Fit of lepton+jets p_T spectrum with gamma × Fermi function.

M_t	p			q			$\chi^2/ndof$	Correlation
160.0	1.08	±	0.09	22.8	±	0.8	2.5	12 %
170.0	0.77	±	0.08	26.6	±	0.9	2.2	9 %
172.5	0.79	±	0.03	26.6	±	0.3	12.4	9 %
180.0	0.78	±	0.07	27.3	±	0.8	1.7	9 %
190.0	0.62	±	0.06	30.6	±	0.9	1.9	7 %

Table 7.4: Fit results for the p_T spectrum of the lepton+jets channel.

a visual improvement of the fit functions compared to the dilepton case although the fit for $M_t = 172.5\,\mathrm{GeV/c^2}$ has a too high $\chi^2/ndof$ of 12.4. Nevertheless the different shown fit functions are clearly distinguishable. The fit functions have a rising amplitude for decreasing mass in the low-p_T region while the tail at high p_T values falls faster for decreasing mass. Numerically the two parameters show a monotonic rise and monotonic fall for rising top quark mass. They are again plotted as a function of the top quark masses of the samples in Figure 7.10. For this channel a dependence on the top quark mass is seen. The simplest approach is to fit a straight line which only has two parameters to the distribution. To reduce the correlation and the dependence on the intercept the distributions were again shifted to their centre of gravity. The fit results are given in Table 7.5.

The χ^2/ndof for parameter p is a bit worse. While the linear dependence seems to be fulfilled in first order, more statistics would be needed to verify it.

Comparing this method with the mean and median value fits, the significance of the slope for parameter q achieves a similar value as the other two methods while

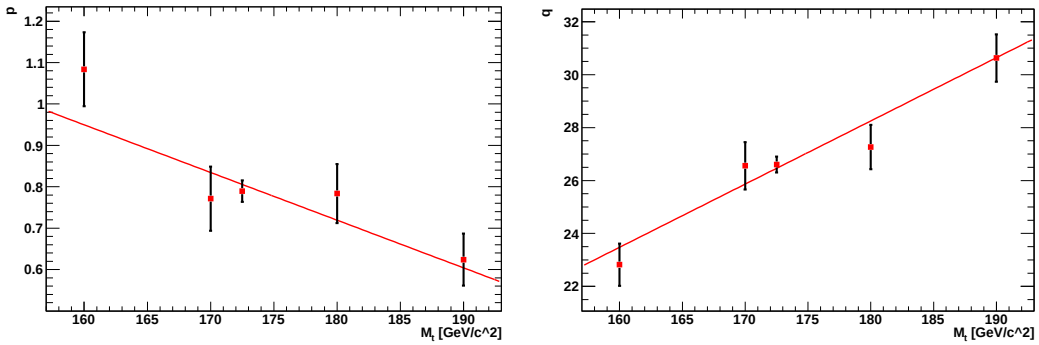

Figure 7.10: Fit parameters p (left) and q (right) of lepton+jets p_T spectrum fit.

	Slope			Intercept			$\chi^2/ndof$
p	-0.0115	$\pm$	0.0031	0.785	$\pm$	0.021	1.4
q	0.239	$\pm$	0.037	26.60	$\pm$	0.24	1.0

Table 7.5: Fit parameters from straight line fit of parameters p and q from the lepton p_T shape fit.

the significance of parameter p is substantially lower and therefore achieves a worse separation of the p_T spectra. To extract a top quark mass one would have to determine the two parameters for ATLAS data and find the most probable top quark mass in the comparison of a two-dimensional parameter space. Such a method would require higher Monte Carlo statistics in the samples, which were not available for this study.

Although a further analysis is not reasonable at this point the evaluation of the lepton+jets channel shows the working concept of this method. The shape fit is able to discriminate the p_T distributions of different top quark masses and a dependence can be concluded. The difference between the lepton+jets and the dileptonic channel implies that the statistics for the application of this method is at the threshold of its feasibility and an increase in luminosity of the Monte Carlo samples could allow a further analysis.

Chapter 8

Summary

In this thesis various methods to measure the top quark mass from the transverse momentum of its decay products applied at the Tevatron collider have been studied to investigate their suitability for the ATLAS experiment. Two different decay channels, the dileptonic decays and the lepton+jets decays, have been selected from Monte Carlo samples with different top quark masses, applying standard cuts. Both electrons and muons were studied independently to allow statements about their respective impact as well as both lepton types together. The selection results were validated with dedicated methods for each channel.

Three different methods to extract the top quark mass were implemented, applied and compared with each other: the fit of the mean leptonic transverse momenta, the fit of the median leptonic transverse momenta and the fit of different transverse momentum spectra. The precision of the mean fit, for an expected integrated luminosity of $200\,\mathrm{pb}^{-1}$ for the first run of LHC, was approximated to an uncertainty on the extracted top quark mass of $11.4\,\mathrm{GeV/c}^2$ for dileptonic and $3.1\,\mathrm{GeV/c}^2$ for lepton+jets decays. The achieved uncertainty for the top quark mass from the median fit is about $5.6\,\mathrm{GeV/c}^2$ for the dileptonic and $3.2\,\mathrm{GeV/c}^2$ for the lepton+jets channel. The overall higher precision is expected from the lepton+jets decays while the median method shows advantages for smaller statistics.

The fit of the lepton transverse momentum spectra was not applicable on the dilepton channel but showed potential separation in the higher statistics lepton+jets decays. An estimate of the achievable precision is more complicated and would require higher Monte Carlo statistics. Overall the mean and median methods show a higher potential with lower complexity.

The analysis has shown that it is possible to measure the top quark mass at the ATLAS experiment with $200\ \mathrm{pb}^{-1}$ with good precision using methods that are independent of the jet energy scale, selection efficiencies and luminosities as they only influence the selection and are not used in the later analysis.

Bibliography

[1] The LEP Electroweak Working Group (online). Available from: `http://lepewwg.web.cern.ch` (Status: 2009-04-08).

[2] J.J. Thomson. Cathode Rays. *Phil. Mag.*, 44:293, 1897.

[3] C. D. Anderson and S. H. Neddermeyer. Cloud Chamber Observations of Cosmic Rays at 4300 Meters Elevation and Near Sea-Level. *Phys. Rev.*, 50(4):263–271, Aug 1936.

[4] M. L. Perl et al. Evidence for Anomalous Lepton Production in $e^+ - e^-$ Annihilation. *Phys. Rev. Lett.*, 35(22):1489–1492, Dec 1975.

[5] M. L. Perl et al. Properties of anomalous e[mu] events produced in e+e- annihilation. *Physics Letters B*, 63(4):466–470, 8 1976.

[6] M. L. Perl et al. Properties of the proposed [tau] charged lepton. *Physics Letters B*, 70(4):487–490, 10 1977.

[7] L. M. Lederman, M. Schwartz, J. Steinberger, et al. Observation of High-Energy Neutrino Reactions and the Existence of Two Kinds of Neutrinos. *Phys. Rev. Lett.*, 9(1):36–44, Jul 1962.

[8] K. Kodama et al. Observation of tau neutrino interactions. *Phys. Lett.*, B504(3):218–224, 2001.

[9] C. L. Cowan, F. Reines, , et al. Detection of the free neutrino: A Confirmation. *Science*, 124:103–104, Jul 1956.

[10] K2K Collaboration, M. H. Ahn, et al. Measurement of Neutrino Oscillation by the K2K Experiment. *Phys. Rev.*, D74:072003, 2006.

[11] G. Zweig. An SU_3 model for strong interaction symmetry and its breaking; Part II. *Cern Report*, CERN-TH-412, Feb 1964.

[12] G. Zweig. An SU(3) model for strong interaction symmetry and its breaking. *CERN-TH-401*, 1964.

[13] M. Gell-Mann. A schematic model of baryons and mesons. *Physics Letters*, 8(3):214–215, 1964.

[14] CDF Collaboration, F. Abe, et al. Observation of Top Quark Production in $p\bar{p}$ Collisions with the Collider Detector at Fermilab. *Phys. Rev. Lett.*, 74(14):2626–2631, Apr 1995.

[15] DØ Collaboration, S. Abachi, et al. Search for High Mass Top Quark Production in $p\bar{p}$ Collisions at $s = 1.8$ TeV. *Phys. Rev. Lett.*, 74(13):2422–2426, Mar 1995.

[16] Particle Data Group, C. Amsler, et al. Review of Particle Physics. *Phys. Lett. B*, 667(1), 2008.

[17] M. Battaglia et al. The CKM Matrix and the Unitarity Triangle. In M. Battaglia, A.J. Buras, P. Gambino, and A. Stocchi, editors, *Proceedings of the First Workshop on the CKM Unitarity Triangle*. CERN, 2003.

[18] M. Kobayashi and T. Maskawa. CP-Violation in the Renormalizable Theory of Weak Interaction. *Progress of Theoretical Physics*, 49(2):652–657, 1973.

[19] S. W. Herb et al. Observation of a Dimuon Resonance at 9.5 GeV in 400-GeV Proton-Nucleus Collisions. *Phys. Rev. Lett.*, 39(5):252–255, Aug 1977.

[20] Tevatron Electroweak Working Group. Combination of CDF and DØ Results on the Mass of the Top Quark. *arXiv*, 0903.2503, Mar 2009.

[21] Tevatron Electroweak Working Group. Combination of CDF and DØ Results on the Mass of the Top Quark. *arXiv*, 0808.1089, Jul 2008.

[22] CDF Collaboration. First direct limit on the top quark lifetime. CDF Conference Note 8104, Feb 2006.

[23] D. Chang, W.-F. Chang, and E. Ma. Fitting precision electroweak data with exotic heavy quarks. *Phys. Rev. D*, 61(3):037301, Jan 2000.

[24] G. Altarelli and G. Parisi. Asymptotic Freedom in Parton Language. *Nucl. Phys. B*, 126:298–318, Aug 1977.

[25] J. Pumplin et al. New generation of parton distributions with uncertainties from global QCD analysis. *Journal of High Energy Physics*, 2002(07):012–012, Aug 2002.

[26] S. Moch and P. Uwer. Heavy-quark pair production at two loops in QCD. *Nucl. Phys. Proc. Suppl.*, 183:75–80, Jul 2008.

[27] J. Campbell and F. Tramontano. Next-to-leading order corrections to Wt production and decay. *Nuclear Physics B*, 726(1-2):109–130, Aug 2005.

[28] Q.-H. Cao, R. Schwienhorst, and C.-P. Yuan. Next-to-leading order corrections to single top quark production and decay at the Fermilab Tevatron: s-channel process. *Phys. Rev. D*, 71(5):054023, Mar 2005.

[29] Q.-H. Cao, R. Schwienhorst, J. A. Benitez, R. Brock, and C.-P. Yuan. Next-to-leading order corrections to single top quark production and decay at the Fermilab Tevatron. II. t-channel process. *Phys. Rev. D*, 72(9):094027, Nov 2005.

[30] Z. Sullivan. Understanding single-top-quark production and jets at hadron colliders. *Phys. Rev.*, D70:114012, Aug 2004.

[31] CDF Collaboration, T. Aaltonen, et al. First Observation of Electroweak Single Top Quark Production. *arXiv*, 0903.0885, Mar 2009.

[32] DØ Collaboration, V. M. Abazov, et al. Observation of single top quark production. *arXiv*, (hep-ex/0903.0850), Mar 2009.

[33] C. Wyss. *LEP design report*, volume 3: LEP2. CERN, Geneva, 1996.

[34] LEP Collaboration. *LEP Design Report*, volume 2 : The LEP main ring. CERN, Geneva, 1984.

[35] M. Benedikt et al. *LHC Design Report*, volume 3: The LHC Injector Chain. CERN, Geneva, 2004. CERN-2004-003-V-3.

[36] O. S. Brüning et al. *LHC Design Report*, volume 1 : the LHC Main Ring. CERN, Geneva, 2004. CERN-2004-003-V-1.

[37] O. S. Brüning et al. *LHC Design Report*, volume 2: the LHC Infrastructure and General Services. CERN, Geneva, 2004. CERN-2004-003-V-2.

[38] ATLAS Photos (online). Available from: `http://atlas.ch/photos/index.html` (Status: 2009-04-08).

[39] ATLAS Collaboration, G. Aad, et al. The ATLAS Experiment at the CERN Large Hadron Collider. *Journal of Instrumentation*, 3(08):S08003, Aug 2008.

[40] ATLAS Collaboration, G. Aad, et al. Expected Performance of the ATLAS Experiment – Detector, Trigger and Physics. *arXiv*, 0901.0512, Jan 2009.

[41] LCG Project: POOL – Persistency Framework (online). Available from: `http://pool.cern.ch` (Status: 2009-04-08).

[42] ROOT – A Data Analyis Framework (online). Available from: `http://root.cern.ch` (Status: 2009-03-28).

[43] SFrame – ROOT NTuple Analysis Framework (online). Available from: `https://twiki.cern.ch/twiki/bin/view/Main/SFramePage` (Status: 2009-03-28).

[44] ATLAS Generators and Interface Documentation (online). Available from: `https://twiki.cern.ch/twiki/bin/view/AtlasProtected/McGeneratorsForAtlas` (Status: 2009-03-27).

[45] Stefano Frixione and Bryan R. Webber. Matching NLO QCD computations and parton shower simulations. *JHEP*, 06:029, Apr 2002.

[46] G. Corcella et al. HERWIG 6.5: an event generator for Hadron Emission Reactions With Interfering Gluons (including supersymmetric processes). *JHEP*, 01:010, 2001.

[47] J. M. Butterworth, J. R. Forshaw, and M. H. Seymour. Multiparton interactions in photoproduction at HERA. *Z. Phys.*, C72:637–646, 1996.

[48] Official web page for TAUOLA PHOTOS and universal interface for TAUOLA (online). Available from: `http://wasm.home.cern.ch/wasm/goodies.html` (Status: 2009-03-27).

[49] S. Agostinelli et al. Geant4 – a simulation toolkit. *Nuclear Instruments and Methods in Physics Research A*, 506(3):250–303, Jul 2003.

[50] J. Allison et al. Geant4 developments and applications. *IEEE Transactions on Nuclear Science*, 53(1):270–278, Feb 2006.

[51] Athena-Atlfast (online). Available from: `http://www.hep.ucl.ac.uk/atlas/atlfast/` (Status: 2009-03-27).

[52] Atlfast II (online). Available from: `https://twiki.cern.ch/twiki/bin/view/Atlas/AtlfastII` (Status: 2009-03-27).

[53] S. Hassani et al. A muon identification and combined reconstruction procedure for the ATLAS detector at the LHC using the (MUONBOY, STACO, MuTag) reconstruction packages. *Nuclear Instruments and Methods in Physics Research Section A: Accelerators, Spectrometers, Detectors and Associated Equipment*, 572(1):77–79, Mar 2007.

[54] N. Giokaris et al. Probing the top-quark mass in the dilepton and lepton + jets channels using only lepton information. JINR-E1-2005-104, Jul 2005.

[55] CDF Collaboration. Measurement of the top quark mass from the lepton transverse momentum in the $t\bar{t} \rightarrow$ dilepton channel at the Tevatron. CDF Conference Note 8959, Aug 2007.

[56] CDF Collaboration. Measurement of the Top Quark Mass with 2.7 fb^1 of CDF Run II Data in the Lepton+Jets Channel using only Leptons. CDF Conference Note 9683, Feb 2009.

[57] F. Garberson et al. Measurement of the Top Quark Mass using Quantities with Minimal Dependence on the Jet Energy Scale. FERMILAB-CONF-08-274-E, Aug 2008.

[58] G. Arabidze et al. Probing the top quark mass in the lepton+jets and dilepton channels by the use of lepton information only. ATL-COM-PHYS-2008-288, Dec 2008.

[59] L. Sachs. *Angewandte Statistik*. Springer-Verlag, Berlin, Heidelberg, New York, 11th edition, 2004.

Acknowledgements

I want to thank Ian Brock for the opportunity to work in his working group and for his constant support also in time-critical periods. I'm very grateful for the countless workshops and conferences he sent me to that enabled me to learn the needed skills for this thesis in a focused way.

I want to thank Balint Radics for helping me to understand the insides of Athena especially in the beginning. It was a good excercise! Peter Kovesarki for the great conversations, for various programming hacks, for creating the Gardener brand, for virtually overcoming the distance between Bonn and CERN and for his constant support through all parts of this thesis. Liz Nuncio and Muhammad Alhroob for enduring my impatience in room 265 and adding fun to everyday work. Big thanks also to Detlef Bartsch who tried to understand the deeper reasons why leptons were so nice to me, for taming the needed statistics and for innumerous suggestions and answered questions.

I want to thank the group members working on real data for teaching me how future work in ATLAS will look like. Melanie Klöß for showing me the PHP universe, Verena Schönberg for sharing my criticism and introducing me to DESY and Hamburg. Michal Wlasenko for his company in the evenings, the spam and his still underestimated contribution to effective meeting management. Ramoona Shehzadi and all colleagues from room 266 for allowing me to finish this work in the ZEUS office. Special thanks to Markus Jüngst for moving to higher energies, for sharing my visions teamwork, for his constant flow of new ideas, for ordering plots and for supporting me when this study needed an end.

I want to thank Markus Cristinziani and his group members for teaming up with us to strengthen top physics in Bonn, for their ideas and input to my analysis, for their expertise and for the fun times we had in Bonn as well as in Hamburg. And also many thanks to Nikos Giokaris and Victoria Giakoumopoulou from Athens University for helping me out with the Gamma $\times$ Fermi fit.

I want to thank the computing team, especially Robert Zimmermann, Thomas Loddenkötter and Gizo Nanava for keeping the infrastructure alive which is so important for analysis work.

I want to thank my parents for believing in me, for all the encouragement and support during my studies. You let a dream become reality. Thanks to Miryam Böhm for all the love, trust and support and to all my family and friends.

Thank you.